

Chiral cavity quantum electrodynamics with coupled nanophotonic structuresFan Zhang,¹ Juanjuan Ren,¹ Lingxiao Shan,¹ Xueke Duan,¹ Yan Li,^{1,4,5} Tiancai Zhang,^{3,4}
Qihuang Gong,^{1,2,4,5} and Ying Gu^{1,2,4,5,*}¹*State Key Laboratory for Mesoscopic Physics, Collaborative Innovation Center of Quantum Matter,
Department of Physics, Peking University, Beijing 100871, China*²*Beijing Academy of Quantum Information Sciences, Beijing 100193, China*³*State Key Laboratory of Quantum Optics and Quantum Optics Devices, Institute of Opto-Electronics,
Shanxi University, Taiyuan 030006, China*⁴*Collaborative Innovation Center of Extreme Optics, Shanxi University, Taiyuan, Shanxi 030006, China*⁵*Frontiers Science Center for Nano-optoelectronics, Peking University, Beijing 100871, China*

(Received 29 October 2018; published 19 November 2019)

Up to now it remains challenging to couple photons from a circularly polarized emitter into a photonic structure to simultaneously realize strong photon-emitter interaction and unidirectional propagation locked by local helicity of the optical mode at the nanoscale. In this paper we propose a unique approach that combines a photonic crystal and metallic nanoparticle structure to create nanocavities with both strong local-field intensity and high helicity. In this system the rate of circularly polarized photons emitting into the photonic crystal waveguide reaches $148\gamma_0$, which is one order of magnitude larger than that without the nanoparticle, and in the ultranarrow band-edge mode the linewidth of Rabi splitting spectra is about one-tenth of that with the nanoparticle only, both with $\approx 95\%$ of photons propagating unidirectionally along the nanoscale waveguide. We suggest that our paper establishes a nanophotonic interface of chiral quantum electrodynamics for on-chip nonreciprocal quantum light sources, quantum circuits, and scalable quantum networks.

DOI: [10.1103/PhysRevA.100.053841](https://doi.org/10.1103/PhysRevA.100.053841)**I. INTRODUCTION**

Cavity quantum electrodynamics (CQED) studies light-matter interaction at a single quantum level [1,2]. With confined electromagnetic fields, optical mode volume and mode density determine the behavior of photon-emitter coupling. By compressing the optical mode into the region of several hundreds of micrometers, weak and strong couplings have been achieved in traditional CQED [3–5]. Recently, through reducing the optical mode volume into micro- and nanoscale, the CQED has succeeded in photonic crystals (PCs) [6,7], plasmonic nanocavities [8–11], whispering guided resonators [12], and various hybrid photonic systems [13–16], which paves the way to nanolasers, on-chip quantum devices, and scalable quantum networks [17]. Besides the ultrasmall mode volume, transversely confined light in photonic structures induces the local helicity of light, the handedness of which has a one-to-one relation to the propagation direction enforced by time-reversal symmetry [18–21]. If one puts a circularly polarized emitter into these structures, the propagation direction of the emitted photons will be locked by the handedness of local spin, the so-called chiral photon-emitter coupling [22,23]. The propagation isolation of photons is able to avoid the signal disturbance and improve transmission efficiency, and hence can be utilized in various nonreciprocal quantum information components, e.g., chiral entanglement [24,25], quantum gates [26,27], switchings [28], isolators [29], and circulators [30].

However, at the nanoscale, the simultaneous realization of the strong interaction between a circularly polarized emitter and cavity photons and the propagation direction lock of photons have not been reported before. Here, we propose nanocavities with strong local field and high helicity in a coupled structure consisting of a W1 PC and Ag nanoparticle (AgNP) [Fig. 1(a)], where the coupling strength of the photon emitter is greatly enhanced and the unidirectional propagation of emitted photons is achieved. Both Purcell enhancement and the vacuum Rabi splitting of chiral coupling are demonstrated at the nanoscale, with $\approx 95\%$ of photons propagating unidirectionally along the nanoscale waveguide in the PC. Moreover, through the mode design, the coupled structure is capable of routing two photons with different wavelength in opposite propagation directions.

In traditional CQED, single-sided cavities with one propagating direction have been reported [31–34]. But the directionality of photons comes from the asymmetric cavity design, so either the right-handed or left-handed photons, provided they are inside the cavity, will be certainly preferentially emitted from the output coupler with high transmission coefficient, while in our design, owing to nonreciprocal properties, emitted photons with opposite handedness will be guided to opposite directions. In whispering gallery resonators [12,30,35], strong chiral photon-atom coupling and nonreciprocal photon propagation are obtained, with which we can realize a single-photon circulator. However, the size of these resonators is microscopic, thus these phenomena occur at the microscale, while in this paper we set up a nanophotonic interface of chiral CQED, where emitted photons propagate along the nanoscale

*ygu@pku.edu.cn

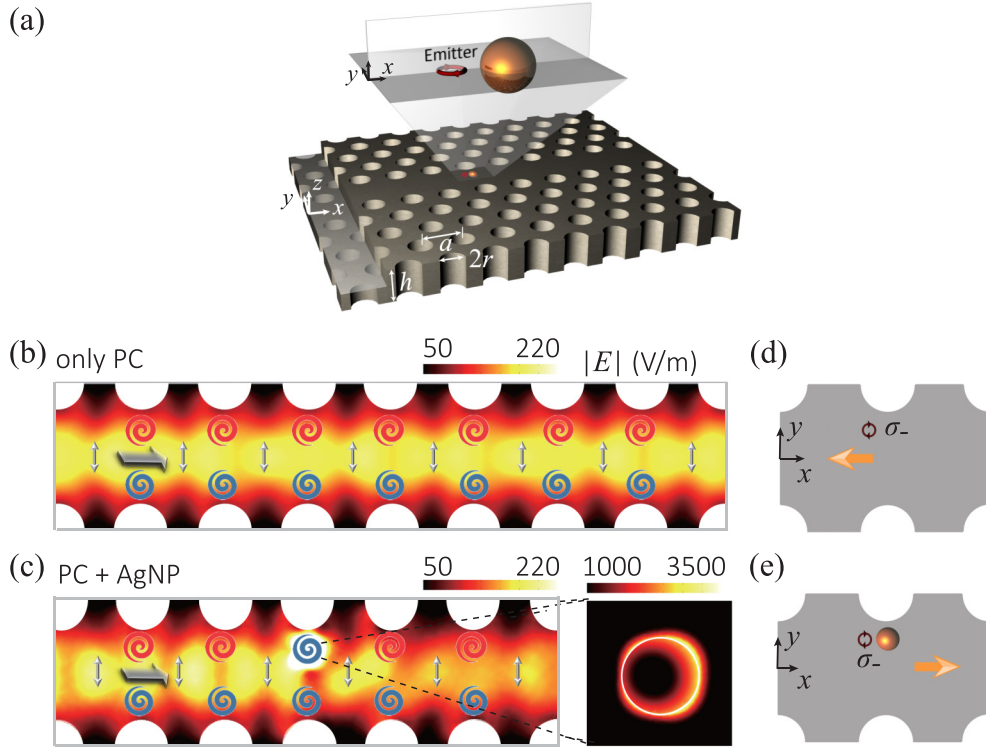


FIG. 1. (a) Schematic diagram of the coupled system with $h = 0.84a$ and $r = 0.29a$. Typical electric-field intensity with colored helical curves of (b) only PC and (c) coupled PC and AgNP structure of the xy plane when the light is incident from the left. Schematic spin-locked photon propagation with (d) only PC and (e) coupled PC and AgNP structure when a σ_- emitter excites their modes, respectively. Here the inset in (c) shows the detailed local field of the AgNP within the area of $80 \times 80 \text{ nm}^2$. The parameters are $a = 190 \text{ nm}$, $r_m = 20 \text{ nm}$, and $a/\lambda = 0.29$, respectively.

waveguide and can be directly used in on-chip nonreciprocal quantum light sources and quantum circuits.

The mechanism of chiral photon-emitter coupling in nano-QED is described as follows. Different from previous chiral coupling at other scales [12,30,35], it is difficult to use an individual nanostructure to realize both strong photon-emitter interaction and high directionality at the nanoscale. The realization of this dual function must rely on optical mode coupling between nanostructures. In traditional mode coupling, researchers generally focus on amplitude superposition after combination of different optical modes, while in order to achieve the above dual goals one must consider a real vector superposition, i.e., the superposition of both the amplitude and the direction between two vectors. Only if both strong local field and high helicity are simultaneously obtained, the above dual function can be realized at the nanoscale.

II. OPTICAL MODES OF COUPLED W1 PC AND AgNP STRUCTURE

Based on the above idea, we choose the coupled PC-AgNP structures to realize both strong photon-emitter interaction and high directionality at the nanoscale. First consider an individual AgNP. If the left-polarized incident light from the $-z$ direction is used to excite a localized surface plasmon of a single AgNP, there is a strong local-field enhancement with nonzero helicity. Typically, the helicity of the z direction is defined as $\frac{2\text{Im}[E_x E_y^*]}{|E_x|^2 + |E_y|^2}$ [36]. As a result, when a σ_- emitter

is located nearby the AgNP, there will be a large Purcell enhancement [8–10]. Secondly, if only a W1 PC is considered, the electric field is mainly located in the waveguide with antisymmetric local helicity distribution [Fig. 1(b)] when light from the x direction is incident on the W1 PC. If now putting a σ_- emitter into the area with red helical curves (such as at the point A or B in Fig. 5 in Appendix B), emitted photons will propagate along the left direction due to the spin-locked direction [19,37–40], i.e., the propagation direction in all areas with red helical curves is connected [Fig. 1(d)]. More details are shown in Appendices A–C.

Then, through the vector coupling between the modes of the PC and AgNP, the typical optical mode possesses both large field enhancement and high helicity around the AgNP, and simultaneous high helicity inside the waveguide channel of the PC [Figs. 1(c) and 1(e)]. Different from only the PC structure, opposite helicity with a blue helical curve appears around the resonant AgNP, as shown in Fig. 1(c). If now one puts a σ_- emitter into the near-field region of the AgNP, both large chiral photon-emitter interaction and unidirectional propagation can be obtained. Specifically, the propagation direction is locked by the sign of local helicity where the emitter is, i.e., the emitted photons will propagate along the right direction [Fig. 1(e)]. Helicity details of the electric field are shown in Fig. 8 in Appendix D. Therefore, with coupled AgNP and PC structure, the chiral interaction is determined by local field while the propagation direction is locked by local helicity.

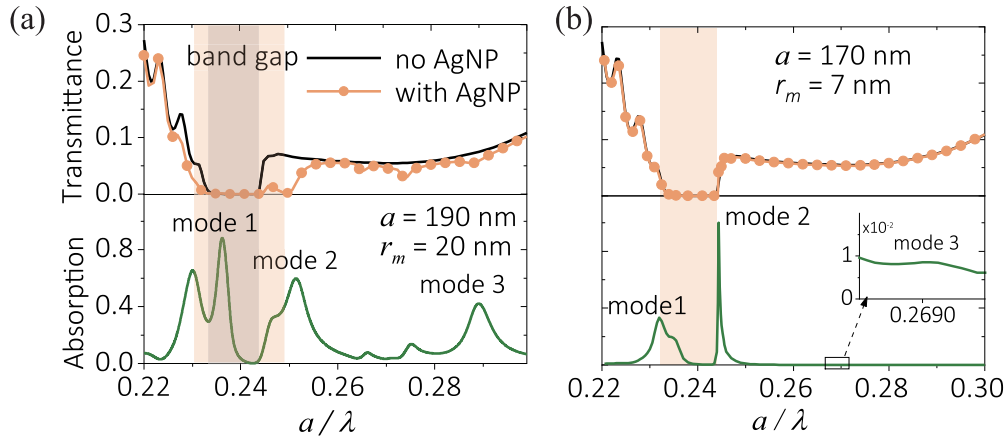


FIG. 2. Optical modes of coupled W1 PC and AgNP structure. Transmittance spectra of the PC and the absorption spectra of the AgNP embedded in the center layer of the PC for (a) $a = 190$ nm and $r_m = 20$ nm and (b) $a = 170$ nm and $r_m = 7$ nm. The center of the AgNP is located at the xy plane with $y = 50$ nm. Here, mode 3 in (a) is prepared for weak coupling while mode 2 in (b) is prepared for strong coupling.

After the mode hybridization of the PC and AgNP, three optical modes arise; i.e., modes 1 and 3 are dipolar and quadrupolar modes of the AgNP, and mode 2 is the band-edge mode [Figs. 2(a) and 2(b)]. Here the W1 PC is chosen with the thickness of $h = 0.84a$, hole radius of $r = 0.29a$, and refractive index of $n = 3.45$, where a is the lattice constant, and computations are performed by the commercial COMSOL and finite-difference time-domain (FDTD) softwares. The process of model coupling is shown in Appendix D. When the radius r_m of the AgNP is 20 nm and $a = 190$ nm, there is a widening of the band gap of the PC due to strong mode coupling between two structures [Fig. 2(a)]. In contrast, as $r_m = 7$ nm and $a = 170$ nm, AgNP size is too small to affect the band of the PC [Fig. 2(b)]. After the parameter optimization, mode 3 in Fig. 2(a) situated at the guided band acts as a nanocavity to provide large Purcell enhancement and effective guidance of photons, while mode 2 in Fig. 2(b) is suitable to realize strong coupling due to its extremely narrow linewidth. In principle, by adjusting geometric and material parameters, the energy bands of the PC as well as the resonance of the plasmon nanoparticle can be modulated to arbitrary electromagnetic frequency.

III. NANOSCALE PURCELL ENHANCEMENT AND UNIDIRECTIONAL PROPAGATION WITH CHIRAL COUPLING

Then, Purcell enhancement of chiral coupling at the nanoscale is demonstrated. After the optimization of position and polarization, we put a σ_- emitter into the near-field region of the resonant AgNP [mode 3 in Fig. 2(a)] with $\lambda = 658$ nm and the distance of $L = 2$ nm. When it circles around the AgNP in the xy plane, i.e., θ is changed from 0° to 360° , the Purcell factor (here normalized total decay rate $\gamma_{\text{tot}}/\gamma_0$) remains at very high values of 4500–4800 [Fig. 3(a)], among which the guided part $\gamma_{\text{WG}}/\gamma_0$ is 95–264 with extreme values corresponding to electric-field maxima of the AgNP. It is noted that the guided part $\gamma_{\text{WG}}/\gamma_0$ is one order larger than $\gamma_{\text{tot}}/\gamma_0$ (≈ 10) of only the W1 PC even at the band-edge region [19,37]. There is also a correspondence between the maximum of directionality D_R and the minimum of decay

rates, where $D_{R \text{ or } L} = \frac{W_{R \text{ or } L}}{W_R + W_L}$ and $W_{R \text{ or } L}$ is the energy power from the emitter into the right or left end of the channel. One can see the computation in Appendix E.

This correspondence can be explained as follows. If the σ_- emitter is placed at the positions with higher helicity, more emitted photons couple to the eigenmode with the same spin, leading to the maxima in the D_R curve. In contrast, if the emitter is located at the lower helicity region, such as for $\theta = 45^\circ$, the directionality D_R is small, but two channels (to left and right directions) can transmit more photons, so the maxima of $\gamma_{\text{WG}}/\gamma_0$ appear. By comparing these curves with Fig. 8 in Appendix E, we prove that a strong local field leads to large Purcell enhancement and high local helicity results in good directionality. Moreover, the metallic loss of the AgNP only influences the Purcell enhancement obviously but not the local helicity, especially within the near-field region of the AgNP (see Appendices E and F). Also, dimer plasmon structure lacks a good directionality due to low helicity originating from the symmetry (see Appendix K).

To balance the inconsistency between the decay rate and directionality, in Fig. 3(b), the parameter of $\theta = 180^\circ$ is chosen. At $\lambda = 658$ nm, both guided Purcell enhancement $\gamma_{\text{WG}}/\gamma_0 = 148$ and the directionality reach very high values. Especially, in the spectral range of 655–661 nm, $\gamma_{\text{tot}}/\gamma_0$ and $\gamma_{\text{WG}}/\gamma_0$ can reach 4200 and 110 and 98% of the guided photons propagate unidirectionally in Appendices G and H. Figures 3(c) and 3(d) depict electric-field and local helicity distributions when the electromagnetic mode is excited by the σ_- emitter with $\lambda = 658$ nm and $\theta = 180^\circ$. As mentioned above, the existence of the AgNP changes the local helicity where the emitter is, thus the propagation direction is opposite to that without the AgNP.

Furthermore, by optical mode design, the coupled structure is capable of separating different wavelength photons into opposite directions. For example, in the above coupled structure, if the AgNP is substituted by a silver nanoblock, two optical modes will appear at different wavelengths. By optimizing the emitter's position near the coupled nanostructure, one can obtain a strong localized field around the corner of the nanoblock but with an opposite sign of field helicity for two modes. If now putting different wavelength σ_- emitters into

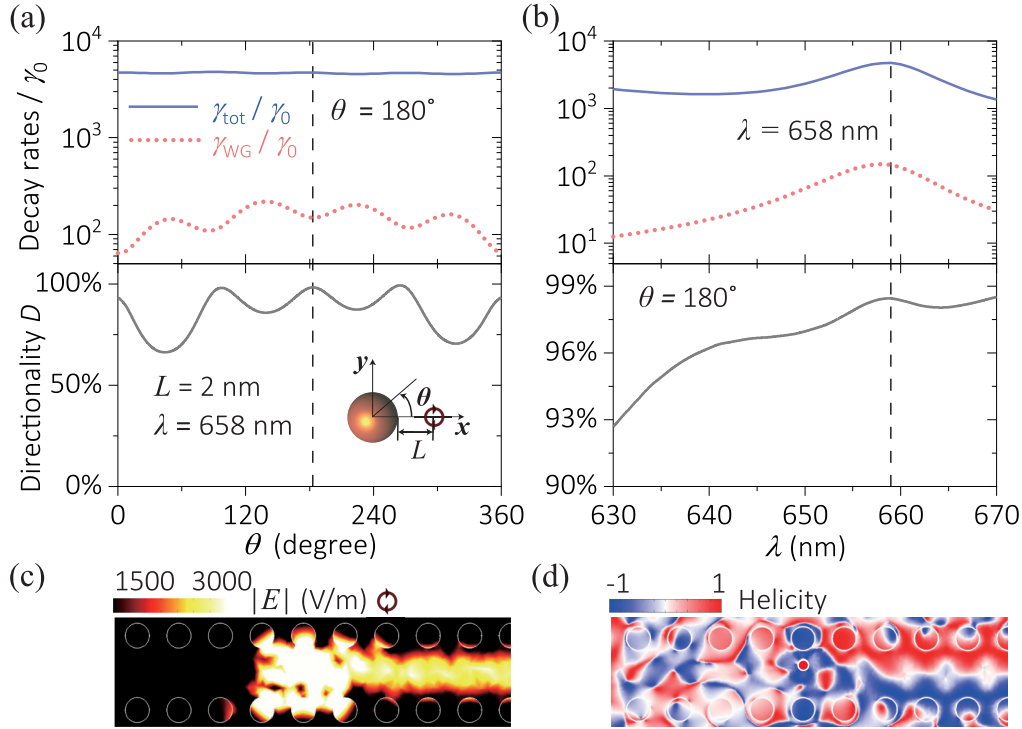


FIG. 3. Nanoscale Purcell enhancement and unidirectional propagation with chiral coupling. Normalized decay rates $\gamma_{\text{tot}}/\gamma_0$ and $\gamma_{\text{WG}}/\gamma_0$ and the directionality D_R as a function of (a) θ and (b) λ . Here we use the quadrupolar mode of the AgNP [mode 3 in Fig. 2(a)] at $\lambda = 658$ nm to realize the chiral coupling and $L = 2$ nm. (c), (d) The distributions of (c) electric field and (d) helicity for $\theta = 180^\circ$ when a σ_- emitter excites the mode of the AgNP.

the optimal position, besides a large Purcell enhancement of emitted photons, the guided parts $\gamma_{\text{WG}}/\gamma_0$ of Purcell factors are steered to the left or right direction separately with high directionality because of the opposite sign of local helicity at these two wavelengths. Therefore, the photons with the same circular polarization will propagate to different directions, which can be utilized to the on-chip routing single-photon source. For more details see Appendix I.

IV. RABI SPLITTING OF FLUORESCENCE SPECTRA AND UNIDIRECTIONAL PROPAGATION WITH CHIRAL COUPLING

Next, the vacuum Rabi splitting of energy levels in chiral coupling is demonstrated. We put the AgNP near the waveguide of the PC [inset of Fig. 4(a)] and demonstrate that the appearance of the band-edge mode is independent of the position of the AgNP in Appendix D. This mode essentially originates from the embedded AgNP that causes the guided mode of the PC to slightly shift below the cutoff region. The AgNP here has two roles, which not only works as a point defect to form a high Q cavity, but also creates a strong helical local field to facilitate strong chiral photon-emitter coupling. It is seen that the mode [mode 2 in Fig. 2(b)] appearing at the edge of the photonic band (with $\lambda = 695.7$ nm) has a very narrow linewidth of $\kappa = 2.9$ meV [Fig. 4(a)], which is only one-tenth of the dipole mode of AgNP in a homogenous medium. Here, $\Delta\lambda \sim 1.13$ nm and its quality factor Q is more than 600. Corresponding to mode excitation, there is an electric-field enhancement inside the PC waveguide, but

the local field around the AgNP is one order stronger than that of the surroundings [Fig. 4(b)]. Then, taking $\theta = 40^\circ$ and 257° as examples, with varying the distance L , coupling coefficients g between the σ_- emitter with dipole moment $\mu = 1.0$ e nm and the nanocavity are shown in Fig. 4(c). For both cases, g decreases exponentially as an increment of L . For example, when $L = 2$ nm and $\theta = 257^\circ$, $g = 3.14$ meV, $\kappa = 2.9$ meV, and the decay rate $\gamma = 0.59$ meV. In this case, the strong-coupling condition $g > (\kappa, \gamma)$ is satisfied [41].

By using the PYTHON toolbox (see Appendix J), fluorescence spectra of the σ_- emitter coupled with the band-edge mode are obtained. Considering that the directionality D_L at $\theta = 257^\circ$ is 94.7% [Fig. 4(d)] and the point M with the frequency detuning $\Delta = \kappa/2$ (between the emitter and cavity mode) is within the guided band of the PC [Fig. 4(a)], we choose the parameters of $\theta = 257^\circ$, $L = 2$ nm, and $\Delta = \kappa/2$. It is found that the Rabi splitting in fluorescence spectra starts to appear at $\mu = 0.5$ e nm and becomes larger with its increment, while for $\mu = 1.0$ e nm there is an apparent energy exchange between the emitter and cavity photons [Fig. 4(e)]. Also, owing to the existence of detuning Δ , the symmetry of fluorescence spectra is broken. The energy splitting and spectral linewidth are roughly coincident with $\sqrt{4g^2 + \Delta^2 - \frac{(\kappa-\gamma)^2}{4}}$ and $\frac{\kappa+\gamma}{2}$ predicted by the dressed state theory [41,42]. The linewidth of fluorescence spectra is about one-tenth of that if only the AgNP. Hence, superior to the individual AgNP, the narrower linewidth of the band-edge mode leads to the earlier appearance of Rabi splitting with the same μ .

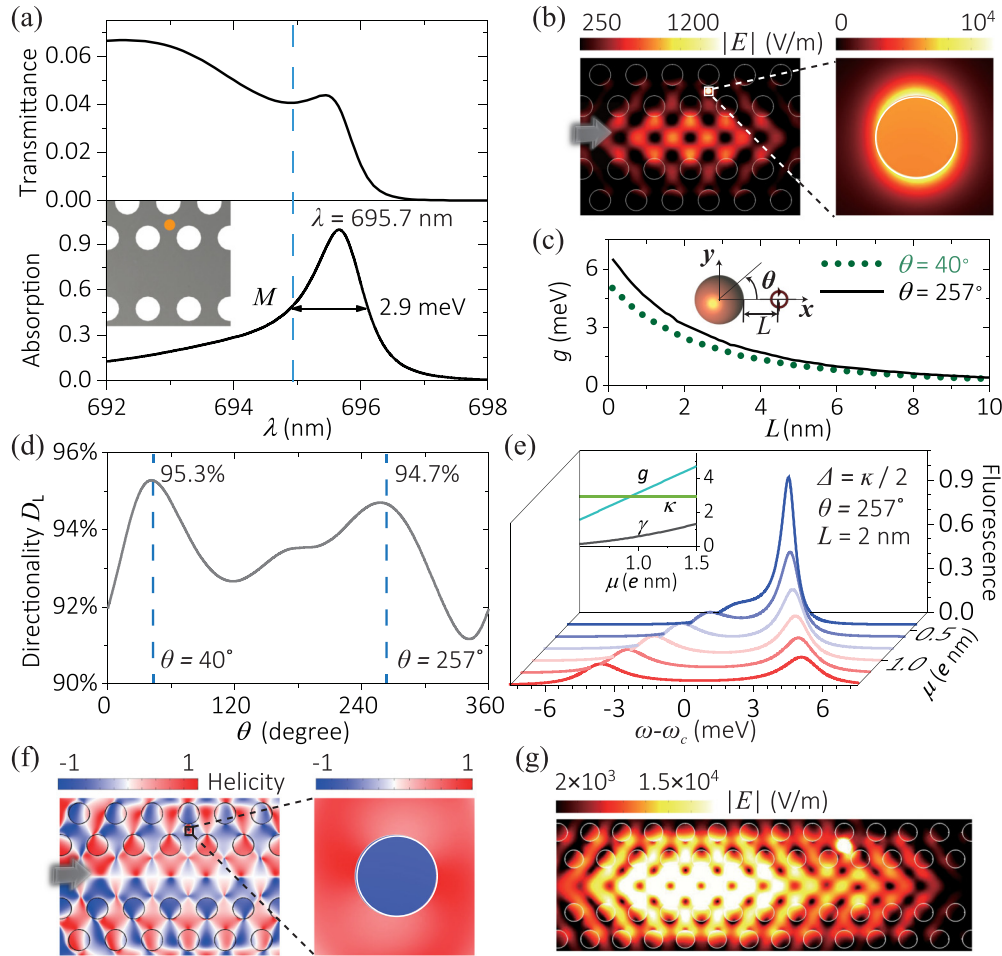


FIG. 4. Rabi splitting of fluorescence spectra and unidirectional propagation with chiral coupling. (a) Transmittance spectra of the PC and absorption spectra of the AgNP [mode 2 in Fig. 2(b)]. (b) The electric-field distributions of the band-edge mode with the insets of the region of 30×30 nm². (c) Coupling coefficient g with varying distance L for $\theta = 40^\circ$ and 257° with $\mu = 1.0$ e nm. (d) Directionality D_L of guided photons with varying θ . (e) Fluorescence spectra of the quantum emitter as a function of $\omega - \omega_c$ with varying μ . The inset shows g , γ , κ dependence on μ . (f) Helicity distribution corresponding to (b). (g) Electric-field distribution for $\theta = 257^\circ$ when the σ_- emitter excites the band-edge mode. In (e) and (g), the detuning $\Delta = \kappa/2$.

In this case, the sign of electric field helicity around the AgNP is opposite to that of only the PC. So, if now putting the σ_- emitter into its near-field region, the photons will be locked to the left direction [Fig. 4(g)]. Compared with the case of $\Delta = 0$, more photons can be transmitted because at the point M the frequency of emitted photons lies in the guided band of the PC. For $L = 2$ nm and $\Delta = \kappa/2$, if letting the emitter walk a circle around the AgNP, the directionality D_L reaches its maximum at $\theta = 40^\circ$ and 257° [Fig. 4(d)]. Corresponding to these maxima, $\approx 95\%$ of guided photons propagate into one direction along the waveguide of the PC, which can be used in nonreciprocal quantum nanophotonic devices [23].

Finally, we address the fabrication possibility of our scheme. Nowadays, a single AgNP [8] and PC [40] can be fabricated by state-of-the-art nanotechnology. If the AgNP is embedded inside the PC, its oxidation or corrosion should be effectively prevented. Also, single emitters embedded in a PC waveguide have been realized through scanning tunneling microscopy [37]. The main challenge to realize efficient chiral coupling is how to precisely control relative positions between

the emitter and AgNP, which may be solved by using an atomic force microscopy tip to move the nanoparticle after emitter position is fixed [43]. By applying a strong magnetic field and selecting laser frequency, we can generate two circularly polarized states $|+\rangle$ and $|-\rangle$ of the atoms [44] or quantum dots [26] to emit only σ_+ or σ_- photons. Thus, it is possible to achieve our scheme experimentally in the near future.

V. SUMMARY

In summary, we have established a nanophotonic interface of chiral CQED by proposing the coupled photonic crystal and plasmon nanoparticle structure. The key element of chiral CQED is the joint action of nanoscale strong local field and high local helicity, which provides strengthened light-emitter coupling with good directionality of emitted photons. Using the basic idea presented here, other kinds of combined nanophotonic structures could be designed, such as a coupled nanowire and nanoparticle system. The study of chiral CQED greatly enriches the understanding of light-emitter

interaction at the nanoscale and provides a possible platform for on-chip quantum light sources, quantum circuits, and scalable quantum networks with nonreciprocal nature.

ACKNOWLEDGMENTS

We thank X. Hu and Y. Ao for helpful discussions. This work is supported by the National Key Research and Development Program of China under Grant No. 2018YFB1107200; by the National Natural Science Foundation of China under Grants No. 11525414, No. 11974032, and No. 11734001; and by the Key Research and Development Program of Guangdong Province under Grant No. 2018B030329001.

APPENDIX A: COMPUTATION MODULE

We use the commercial COMSOL multiphysics software to perform the simulations. The TE-like PC, containing 11×12 unit cells shown in Fig. 5(a), is placed in the middle of a three-

dimensional module with the height of $h + 1 \mu\text{m}$ [Fig. 5(b)]. To minimize boundary reflections and form an infinite space, the scattering boundary condition is used to surround the module. An AgNP, the permittivity of which is taken from the experimental data [45], is embedded in the middle plane of the waveguide of the PC. Adding an incident plane wave propagating along the x axis, or putting an oscillating point dipole inside the PC, modes of the coupled PC and AgNP structure can be excited.

The circular polarization of the light is represented by helicity, which is defined as [36]

$$C = \frac{|E_{\text{LCP}}|^2 - |E_{\text{RCP}}|^2}{|E_{\text{LCP}}|^2 + |E_{\text{RCP}}|^2}, \quad (\text{A1})$$

where E_{LCP} (E_{RCP}) is the left (right) component of the electric field related to the basis. If we choose the basis of $\frac{\hat{x}+i\hat{y}}{\sqrt{2}}$, $\frac{\hat{x}-i\hat{y}}{\sqrt{2}}$, and \hat{z} , the helicity in the z direction can be written as $C(z) = \frac{2\text{Im}[E_x E_y^*]}{|E_x|^2 + |E_y|^2}$. In the same way, we can derive $C(x) = \frac{2\text{Im}[E_y E_z^*]}{|E_y|^2 + |E_z|^2}$

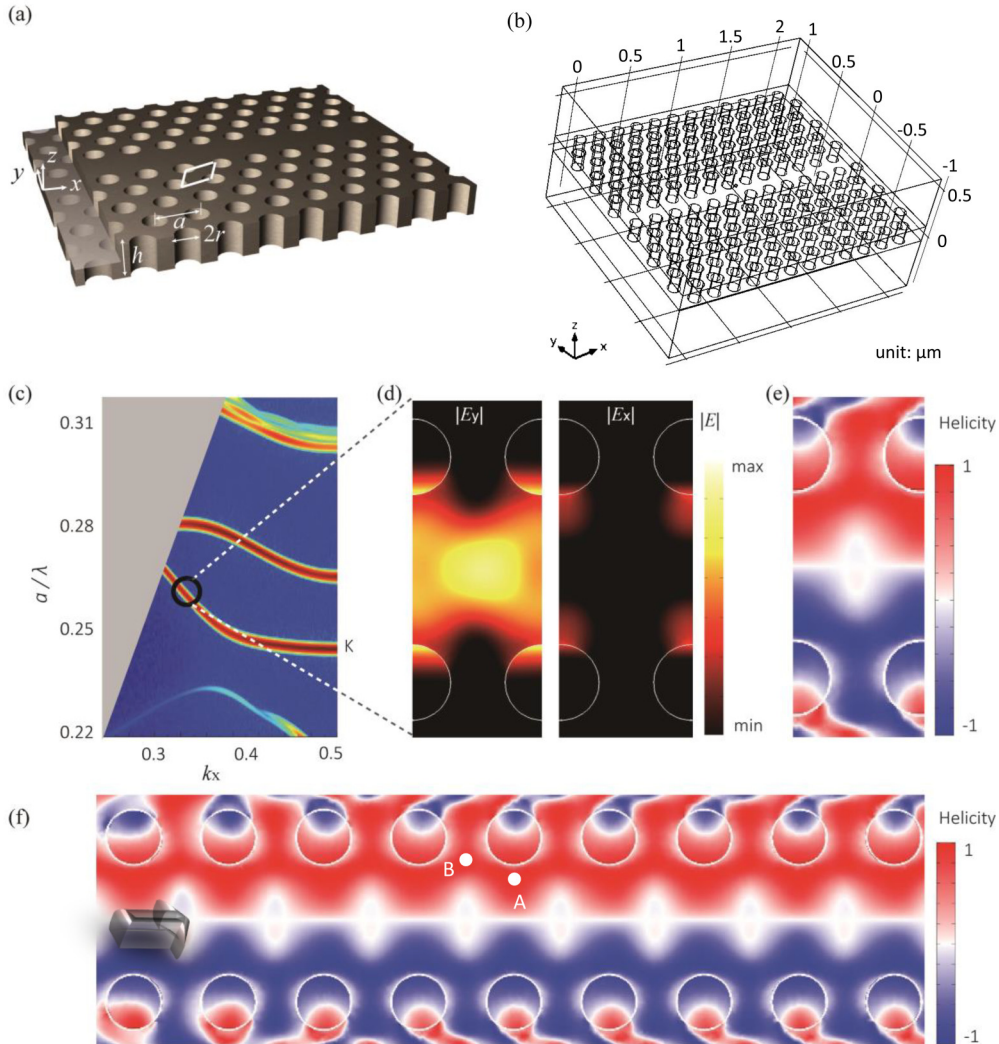


FIG. 5. (a) Schematic diagram of the W1 PC and (b) computation module of COMSOL software. One unit cell of the PC is marked within the white lines in (a). (c) Photonic band diagram for the period of $a = 190 \text{ nm}$, the hole radius of $r = 0.29a$, the thickness of $d = 0.84a$, and the refractive index of $n = 3.45$. (d) The electric-field components $|E_x|$ and $|E_y|$ and (e) helicity distributions of the z direction when $a/\lambda = 0.26$. (f) The electric-field distribution in the waveguide of the W1 PC. The electric fields are normalized by the maximum of $|E_y|$.

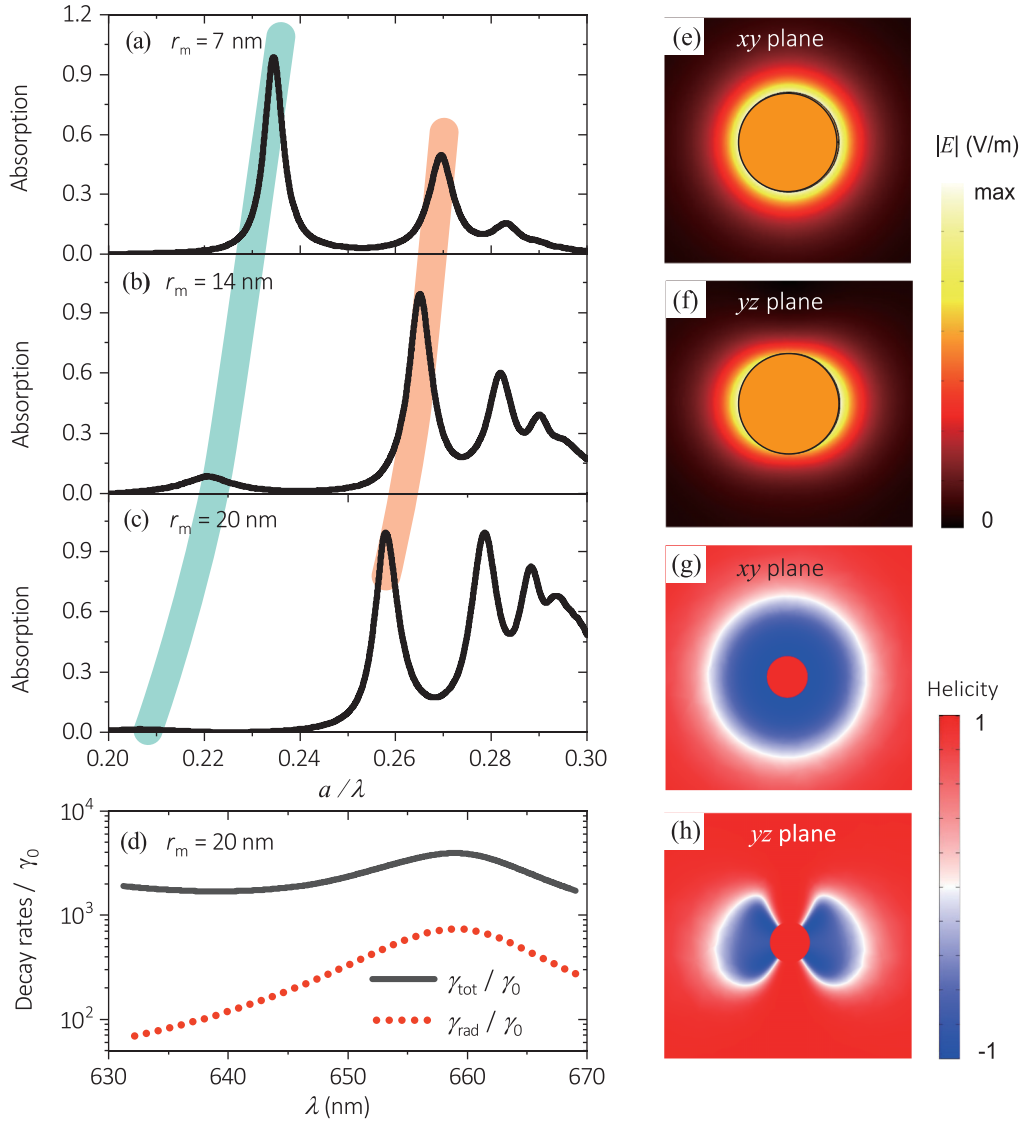


FIG. 6. Absorption spectra of the AgNP in a homogeneous medium with refractive index of $n = 3.45$, for the radius of (a) $r_m = 7$ nm, (b) $r_m = 14$ nm, and (c) $r_m = 20$ nm. The wavelength is normalized by $a = 170$ nm to compare with the case of the AgNP embedded in the PC waveguide. For the AgNP with different size, redshift of resonance wavelength occurs as r_m enlarges. (d) Purcell enhancement of the σ_- emitter near the AgNP embedded in a homogeneous medium. Here $r_m = 20$ nm, $n = 3.45$, and the distance between them is 2 nm. (e), (f) The electric-field distributions and (g), (h) helicity distributions of the dipole mode of a AgNP with $r_m = 7$ nm in the xy and yz planes. A left-handed polarized plane wave is used to excite the AgNP, which propagates along the $-z$ direction.

and $C(y) = \frac{2\text{Im}[E_z E_x^*]}{|E_z|^2 + |E_x|^2}$. From Eq. (A1), $C = 1$ represents the left-polarized light and $C = -1$ is the right-polarized light. In the COMSOL module, the left- and right-handed polarized plane waves along the z axis are given as $\vec{E}_{\pm} = E_x \hat{x} + E_y \hat{y} = \frac{E_0 \hat{x} + E_0 e^{\mp\pi/2} \hat{y}}{\sqrt{2}}$, where E_0 is the amplitude of the electric field and E_y is $\pm\pi/2$ out of phase with E_x . Similarly, the left- and right-handed polarized emitters are set as oscillating point dipoles for $\sigma_{\pm} = \frac{\mu \hat{x} + \mu e^{\mp\pi/2} \hat{y}}{\sqrt{2}}$, where μ is the magnitude of the dipole moment. The transmittance spectrum of the PC is defined as I_t/I_0 , where I_t and I_0 are the light intensity in the incident and exit surfaces of the PC. In this paper, the light is incident on the left end of the PC and the right end is used as the receiving surface to collect photons.

APPENDIX B: PHOTONIC BAND DIAGRAM OF THE PHOTONIC CRYSTAL

We compute the photonic band diagram of the W1 PC by a FDTD method with commercial software (LUMERICAL) [Fig. 5(c)]. To reduce the computation process, a two-dimensional module, where the thickness of the PC is represented by a modified refractive index n_{eff} , is performed. Through boundary mode analysis in the COMSOL module, we obtain $n_{\text{eff}} = 2.95$. Compared with the transmittance spectra in Figs. 2(a) and 2(b), the band gap in Fig. 5(c) is coincident with that in the transmittance spectra obtained by COMSOL software. Typical distributions of the electric field and its helicity inside the waveguide of the PC are shown, respectively, in Figs. 5(d) and in Figs. 5(e) and 5(f).

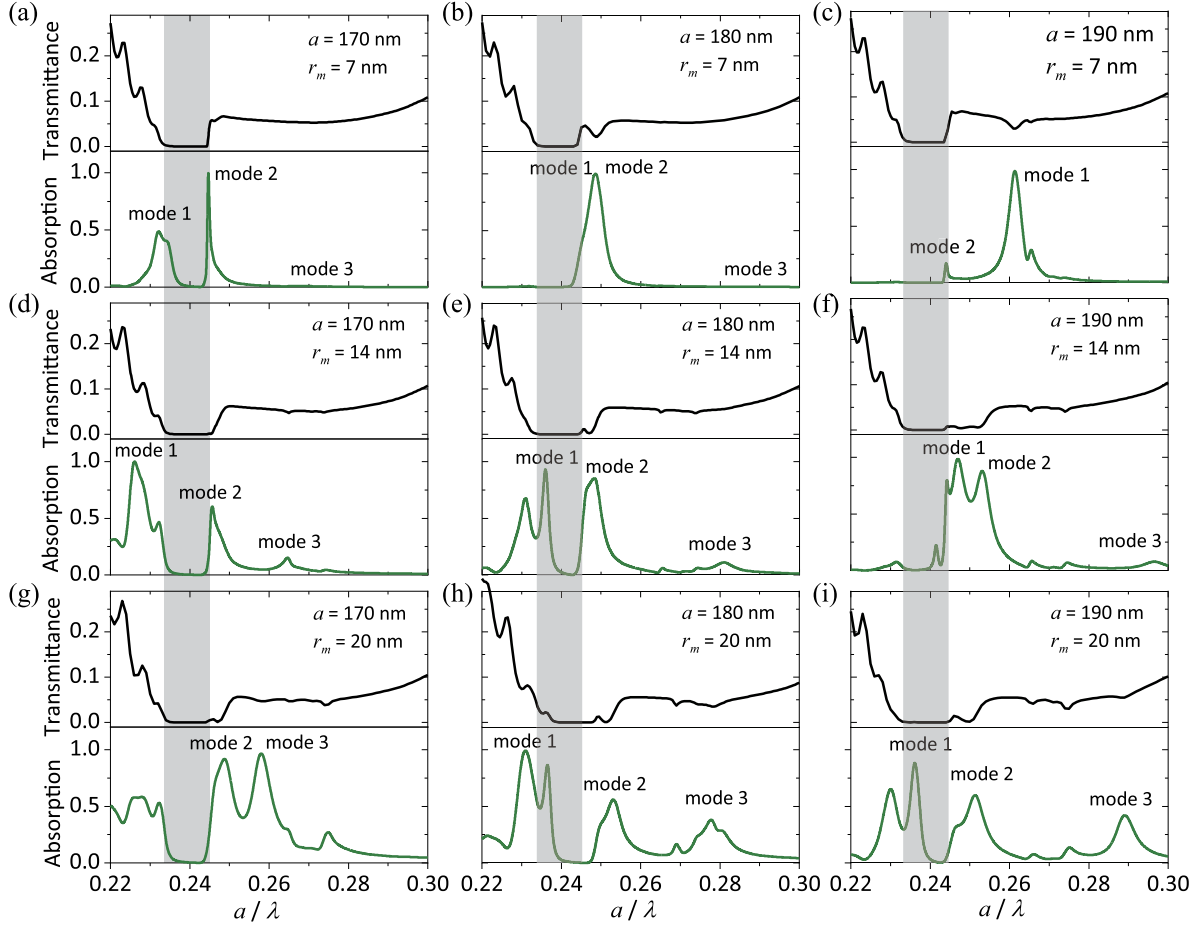


FIG. 7. The transmittance spectra of the PC and the normalized absorption spectra of the AgNP with the radius of (a)–(c) $r_m = 7$ nm, (d)–(f) $r_m = 14$ nm, and (g)–(i) $r_m = 20$ nm. The parameters for $a = 170$ – 190 nm are computed to change optical modes hybridized by the PC and AgNP. Figures 2(a) and 2(b) in the main text correspond to (i) and (a), respectively, and the band gap of a PC without the AgNP is shown as the gray region. Mode 1 and mode 3 are the dipole and quadrupole modes of the AgNP and mode 2 is the band-edge mode corresponding to the K point in the band diagram of Fig. 5(c). By increasing the radius of the AgNP, the band-edge mode always exists and its gap width enlarges. Specifically, when $a = 180$ nm and $r_m = 7$ nm, mode 1 lies at the band edge of the PC so that modes 1 and 2 are almost overlapped.

APPENDIX C: THE ELECTRIC FIELD AND ITS HELICITY FOR THE MODES OF THE AgNP

In the following, we analyze the electric field and its helicity for the mode of the AgNP in a homogeneous medium with the refractive index of $n = 3.45$. The absorption spectra of the AgNP for different radii r_m are shown in Figs. 6(a)–6(c). As r_m enlarges, redshift in the resonance wavelength occurs. When $r_m = 20$ nm, $n = 3.45$, and the distance between the emitter and AgNP is 2 nm, Purcell enhancement of the σ_- emitter near the AgNP embedded in the homogeneous medium is displayed in Fig. 6(d). Figures 6(e)–6(h) depict the electric-field and helicity distributions of the AgNP in the xy and yz planes, respectively. A left-handed plane wave of $\lambda = 625$ nm polarized in the xy plane is used to excite the dipole mode of the AgNP with the radius of 7 nm. It is seen that the electric field in the yz plane is similar to that of a linearly polarized dipole in the y direction, while in the xy plane the absolute value of the electric field is homogeneous around the AgNP. Note, the helicity around the AgNP in the xy plane has an opposite sign against that of the excited light.

This phenomenon can be explained as follows. The equivalent dipole moment of the AgNP excited by a plane wave with $\vec{E} = [1, i, 0]E_0e^{-i(k_z z - \omega t)}$ is given as

$$\vec{p}_{\text{MNP}} = 4\pi\epsilon_b\epsilon_0r_m^3\Gamma(E_0\hat{x} + iE_0\hat{y}), \quad (\text{C1})$$

where $\Gamma = (\epsilon_m - \epsilon_b)/(\epsilon_m + \frac{n'+1}{n'}\epsilon_b)$ with the permittivity ϵ_m of the AgNP and ϵ_b of the host medium [46]. Take the dipole mode as an example, namely, $n' = 1$, $\Gamma = (\epsilon_m - \epsilon_b)/(\epsilon_m + 2\epsilon_b)$, and the resonant condition is $\epsilon_m = -2\epsilon_b$. Under the resonant condition, $[p_x, p_y] \propto [-i, 1]$, which has the same form as that of a σ_- emitter the near field of which has positive helicity in the yz plane. Similarly, the local polarization of the higher-order modes of the AgNP has the same sign as that of the dipole mode.

APPENDIX D: OPTICAL MODE COUPLING IN THE COUPLED PC AND AgNP STRUCTURE

The transmittance spectra of the PC and the absorption spectra of the AgNP with various radii r_m and lattice constants a are shown in Fig. 7. The gray region is the band gap of the

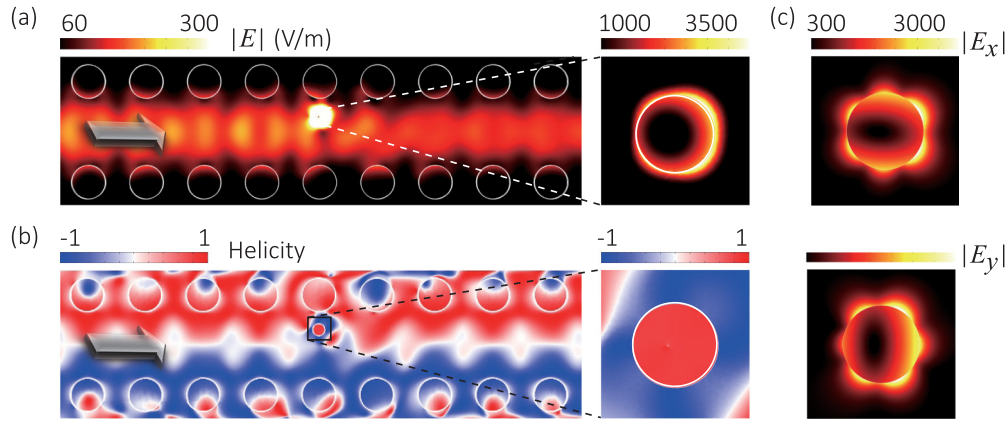


FIG. 8. (a) The electric-field and (b) its helicity distributions of the xy plane in the PC with the existence of the AgNP, where the arrows depict the propagation direction of the light. The insets show the details near the AgNP within the area of 80×80 nm. (c) The electric-field components $|E_x|$ and $|E_y|$ within the area of 80×80 nm² in the coupled PC and AgNP structure. The parameters are set as $a = 190$ nm and $r_m = 20$ nm.

PC without the existence of the AgNP. We can see that the band gap is broadened as the radius r_m of the AgNP enlarges. As in Figs. 2(a) and 2(b), mode 1 and mode 3 correspond to the dipole and quadrupole modes of the AgNP and mode 2 is a band-edge mode [43,47]. Here, lattice constant a is changed to make the mode of the AgNP situate at different frequency regions of the PC, i.e., guided and band-gap regions. Take $r_m = 7$ nm, for example. As a increases, the dipole mode of the AgNP moves from the band gap to the guided band of the PC. Comparing Figs. 7(a)–7(c), it is seen that narrow and sharp band-edge modes appear when the dipole mode of the AgNP locates at the band gap of the PC [Fig. 7(c)]. Redshift in the absorption spectra is also clearly shown as an increment of r_m .

For a single AgNP, a single PC, and the coupled AgNP and PC structure, the helicity distributions in the xy plane are depicted in Figs. 6(f), 5(e), and 8(b), respectively. The signs of helicity between the excited AgNP and the external field are opposite [Fig. 6(f)]. If the AgNP is embedded in the PC, the hybrid mode has opposite spin against that without the AgNP [Figs. 8(b) and 5(e)]. The electric-field and helicity distributions of the hybrid mode within an area of 80×80 nm² are shown in Fig. 8. As seen in Fig. 8, the merit of the hybrid mode is illustrated by not only electric-field enhancement, but also the control and adjustment of the spin, which can be used to modulate both spontaneous emission of the emitter and the propagation direction of photons.

Finally, by adjusting geometric and material parameters, the energy bands of the PC as well as the resonance of the plasmon nanoparticle can be modulated to arbitrary electromagnetic frequency. For example, by reducing a with fixed ratios $h = 0.84a$ and $r = 0.29a$, the transmittance spectrum can be moved to the UV region, and simultaneously the UV resonance of the Al nanoparticle [48] can be designed within the guided band or band edge of the PC. If now putting the Al nanoparticle into the waveguide of the PC and optimizing the parameters of the coupled system, the high directionality as well as large Purcell enhancement in the UV region should also be achieved.

APPENDIX E: COMPUTATION OF VARIOUS COEFFICIENTS

Three physical processes are included in the CQED systems: the coupling between the cavity photons and emitter, the decay of the emitter, and the cavity loss, the coefficients of which are labeled as g , γ , and κ , respectively. According to their relations, two typical regimes exist, i.e., weak coupling for $g \ll \gamma, \kappa$ and strong coupling for $g \gg \gamma, \kappa$ [3].

1. Weak coupling

In the weak-coupling regime, the emitter decays through three channels: guided along the waveguide γ_{WG} , radiating into the far field γ_{free} , and nonradiative loss γ_{NR} . Thus the total decay rate γ_{tot} is equal to the sum of these decay rates, i.e., $\gamma_{\text{tot}} = \gamma_{\text{WG}} + \gamma_{\text{free}} + \gamma_{\text{NR}}$. The total normalized decay rate can be obtained from $\gamma_{\text{tot}}/\gamma_0 = W_{\text{tot}}/W_0$ [49], where W_{tot} and W_0 are the total emitted energy power of an emitter in the coupled system and in vacuum, respectively. The energy power of the emitter in the COMSOL module is given by the surface integration of a nanosphere containing the emitter over the energy flows, which can be expressed by $W_{\text{tot}} = \iint_{\Sigma} \vec{S} \cdot d\Sigma$, and \vec{S} is the Poynting vector on the nanosphere [15]. Similarly, the guided part along the waveguide is calculated by $\gamma_{\text{WG}}/\gamma_0 = W_{\text{WG}}/W_0$, where W_{WG} is the energy power of summing over receiving surfaces, i.e., right and left surfaces of the module.

2. Strong coupling

The emitter-nanocavity coupled system in the strong-coupling regime can be represented by the Jaynes-Cummings model, where the Hamiltonian and dynamical equation are

$$H = \omega_c \sigma_+ \sigma + \omega_c a^\dagger a + g(\sigma_+ a + a^\dagger \sigma) \quad (\text{E1})$$

and

$$\begin{aligned} \dot{\rho} = & i[\rho, H]/\hbar + \frac{\gamma}{2}(2\sigma \rho \sigma^\dagger - \{\sigma^\dagger \sigma, \rho\}) \\ & + \frac{\kappa}{2}(2a \rho a^\dagger - \{a^\dagger a, \rho\}), \end{aligned} \quad (\text{E2})$$

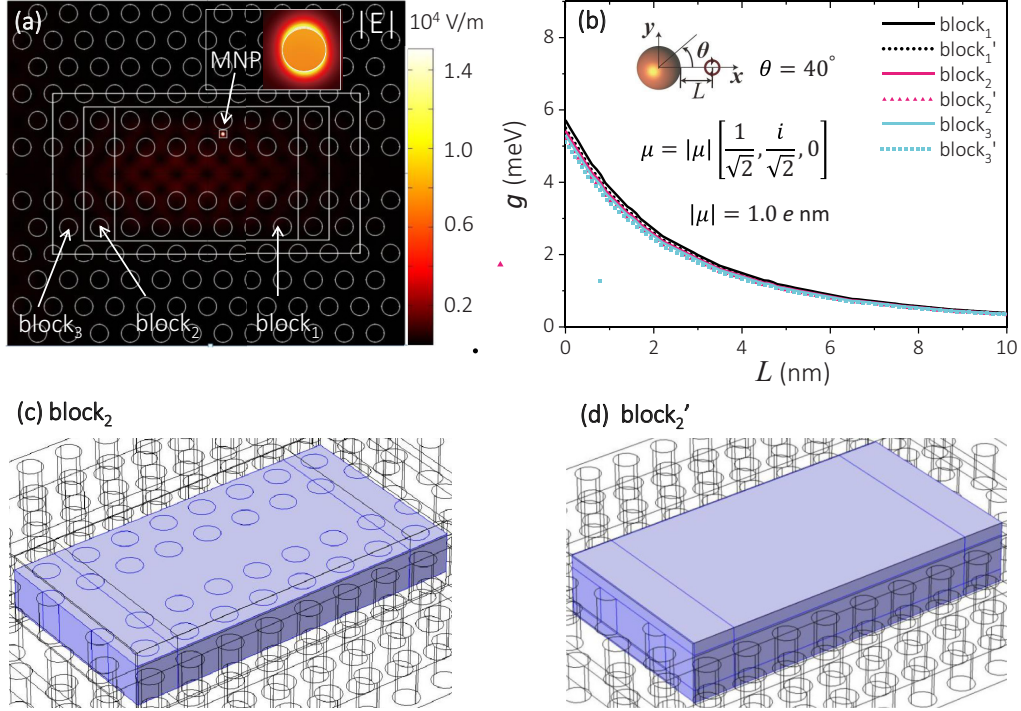


FIG. 9. (a) Electric-field distribution of the nanocavity in coupled photonic nanostructures. Three different extracted energy regions are marked with white lines. Their sizes are $6a \times 4.33a \times h$, $8a \times 4.33a \times h$, and $10a \times 5.20a \times h$ for $block_1$, $block_2$, and $block_3$, respectively. Based on these three regions, we add 50-nm-thick air layers above and below to form three new regions, the sizes of which are $6a \times 4.33a \times (h + 100 \text{ nm})$, $8a \times 4.33a \times (h + 100 \text{ nm})$, and $10a \times 5.20a \times (h + 100 \text{ nm})$ for $block_1'$, $block_2'$, and $block_3'$. (b) Comparison of coupling coefficients with various integration ranges. These values are very close. (c) $Block_2$. (d) $Block_2'$.

where ω_e and ω_c are the frequencies of the emitter and the nanocavity, respectively; σ (σ^+) is the lowering (raising) operator of the emitter; and a (a^+) is the bosonic annihilation (creation) operator of the nanocavity. The physical process in this system is that the emitter and nanocavity exchange energy with coupling coefficient g , and, simultaneously, photons also decay because of the atomic decay and Ohmic loss of the cavity, with coefficients labeled as γ and κ . In the following, we will show how to compute these coefficients by means of COMSOL software.

a. Coupling coefficient g

Following the equations and method in Refs. [16,50], $\hbar g = \mu E_s$ where E_s is the electric field of the nanocavity corresponding to a single excitation and can be written as

$$E_s = \tilde{E} / \sqrt{\frac{W}{\hbar\omega_c}}, \quad (\text{E3})$$

where \tilde{E} is the excited electric field of the nanocavity, $\sqrt{\frac{W}{\hbar\omega_c}}$ denotes the number of photons with energy $\hbar\omega_c$, and W is the total energy of the cavity mode which is calculated by energy density integration in the whole space [16]:

$$W = \frac{1}{2} \int \frac{\partial}{\partial \omega} \{ \omega \text{Re}[\varepsilon(\omega)] \} |_{\omega=\omega_c} |\tilde{E}|^2 dV + \frac{1}{2} \int \mu_0 |\tilde{H}|^2 dV. \quad (\text{E4})$$

In the following, we will verify the correctness of the coupling coefficient calculation. As mentioned above, W is

the total energy of the cavity mode which is calculated by energy density integration in the whole space. But in fact, when the integration range is large enough, the energy obtained is close to the total energy W and the resulting coupling coefficient approaches the true value. Here, the considered nanocavity is a hybrid cavity formed by the interaction of the AgNP and the PC [corresponding to mode 2 in the main text of Fig. 2(b)]. Electric-field distribution of this nanocavity is shown in Fig. 9(a). In addition to strong local fields near the nanoparticles, there is also a large field distribution near the PC waveguide. Three different extracted energy regions are marked with white lines in Fig. 9(a). Their sizes are $6a \times 4.33a \times h$, $8a \times 4.33a \times h$, and $10a \times 5.20a \times h$ for $block_1$, $block_2$, and $block_3$, respectively. It is worth mentioning that energy is not only localized in the PC layer, but also a small amount of energy exists in the air layer above and below the PC layer. Thus based on those three regions, add 50-nm-thick air layers above and below to form three new regions. Their sizes are $6a \times 4.33a \times (h + 100 \text{ nm})$, $8a \times 4.33a \times (h + 100 \text{ nm})$, and $10a \times 5.20a \times (h + 100 \text{ nm})$ for $block_1'$, $block_2'$, and $block_3'$, respectively. In particular, the regions of $block_2$ and $block_2'$ are shown in Figs. 9(c) and 9(d). Finally, comparison of coupling coefficients obtained by various ranges of extracted energy is shown in Fig. 9(b). These coupling coefficients are very close, which means that these ranges are large enough that coupling coefficients are very close to true value. In the main text, the coupling coefficients are obtained by energy integration in the range of $block_2'$.

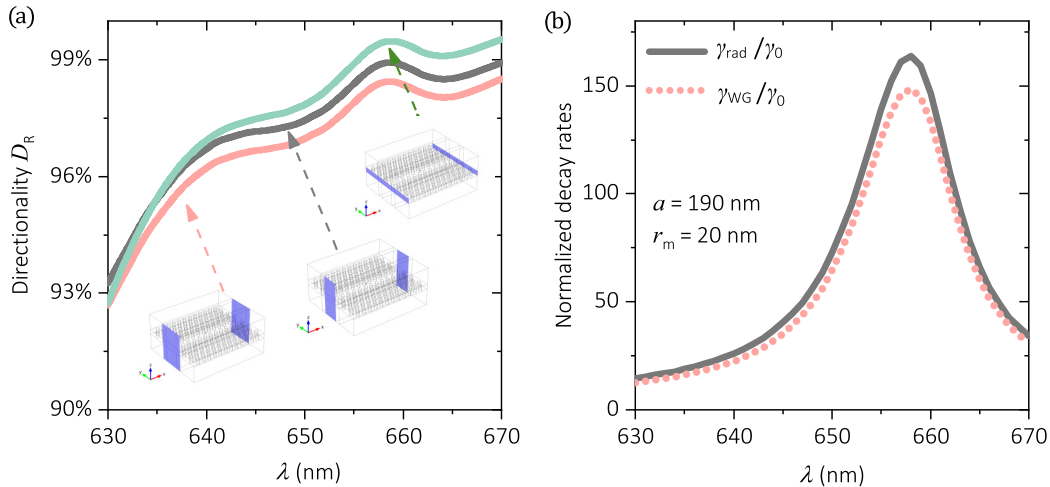


FIG. 10. (a) Directionality of the photons emitted from a σ_- emitter for different receiving surfaces to collect photons. The receiving surfaces are shown as the insets. Because the photons lose the lock of propagation direction in the free space, directionality D_R reduces a little when the surrounding environment is involved. However, the wavelengths of the maxima in these three cases are not changed. Here, the emitter is set at $y = 50$ nm. (b) Normalized decay rate of the σ_- emitter in the coupled PC and AgNP structure for the radiative part ($\gamma_{\text{rad}}/\gamma_0$) and along the waveguide ($\gamma_{\text{WG}}/\gamma_0$). More than 90% of the radiative photons are coupled to the waveguide of the PC. Other parameters are the same as those in Fig. 3.

b. Cavity loss κ

The cavity loss κ is the full width at half maximum (FWHM) of its extinction spectra, including the scattering and absorption of the cavity. Because the FWHMs of scattering and absorption spectra are almost the same [51], κ is derived from the absorption spectrum here. In the COMSOL module, the mode of the AgNP is excited by a nearby oscillating point dipole. By volume integrating the AgNP over the power density, the resistive loss W_{NR} is obtained. κ of the AgNP in the homogeneous environment with refractive $n = 3.45$ can be obtained in Figs. 6(a)–6(c). Using the same procedure, κ of the AgNP in the PC can be obtained, too.

c. Decay rate γ

Decay rate γ here indicates the atomic decay rate to the modes other than the cavity mode, i.e., except for the nonradiative decay caused by the loss of the AgNP. Therefore, γ is equal to the total decay rate minus the nonradiative part, i.e., $\gamma = \gamma_{\text{tot}} - \gamma_{\text{NR}}$, which can be obtained by $\gamma = \frac{W_{\text{tot}} - W_{\text{NR}}}{W_0} \gamma_0$ and $\gamma_0 = \omega^3 \mu^2 / 3\pi \epsilon_0 \hbar c^3$ [52].

APPENDIX F: COMPUTATION OF DIRECTIONALITY FOR PHOTON PROPAGATION

We compare the directionality with different areas of the receiving surface of the module. Figure 10(a) depicts the directionality D_R with the size of the receiving surface of $3.5\sqrt{3}a \times (h + 1 \mu\text{m})$, $1.5\sqrt{3}a \times (h + 1 \mu\text{m})$, and $6.5\sqrt{3}a \times h$, respectively. Because the photons lose the lock of propagation direction in the free space, directionality reduces when the surrounding environment is involved. However, the differences in these three cases are small and the wavelengths of the maxima in these three cases are not changed. So, in the main text, the area of $3.5\sqrt{3}a \times (h + 1 \mu\text{m})$ is used. In this

case, more than 90% of the radiative photons are coupled to the waveguide of the PC [Fig. 10(b)].

To investigate the effect of metallic loss to the Purcell enhancement and directionality of photon propagation, we give the absorption spectra, directionality D_R , and normalized decay rate $\gamma_{\text{WG}}/\gamma_0$ for different loss rates [Fig. 11(a)]. By keeping the real part $\text{Re}[\epsilon_m]$ of the dielectric constant as the original value for each wavelength, we artificially increase the imaginary part $\text{Im}[\epsilon_m]$ by a factor of 1, 2, and 3. It is found that increasing the loss of metal material does not obviously affect the peak position and directionality, but does affect the Purcell enhancement. The reason is that the local electric field determines the Purcell enhancement, which is greatly influenced by the metallic loss, while the directionality of photon propagation comes from the local helicity, which is not greatly affected by the metal loss, especially within the near-field region of the AgNP [Figs. 11(c)–11(e)]. Other parameters in Fig. 11 are the same as those in Fig. 3.

APPENDIX G: PURCELL FACTOR AND PROPAGATION DIRECTIONALITY WHEN AN EMITTER COUPLES TO ONLY THE PC

First, we discuss the Purcell enhancement of a circularly polarized emitter coupled to a PC. Some experimental and theoretical works show that the Purcell factor in the slow-light region of the PC can reach 10 as well as the directionality over 90% [19]. Here, we put a right-handed polarized emitter σ_- in the PC with $y = 50$ nm [Fig. 12(a)] and $y = 0$ [Fig. 12(b)], then obtain the decay rate of the emitter and directionality of the emitted photons. As shown in Fig. 12, the total decay rate in both cases has an increment at the band edge of the PC, namely, in the slow-light region [Fig. 5(c)]. In this region, the gradient of the energy band is very small, so the group velocity of the photons is also slow [19,40]. That is why the emitter has large Purcell enhancement at the

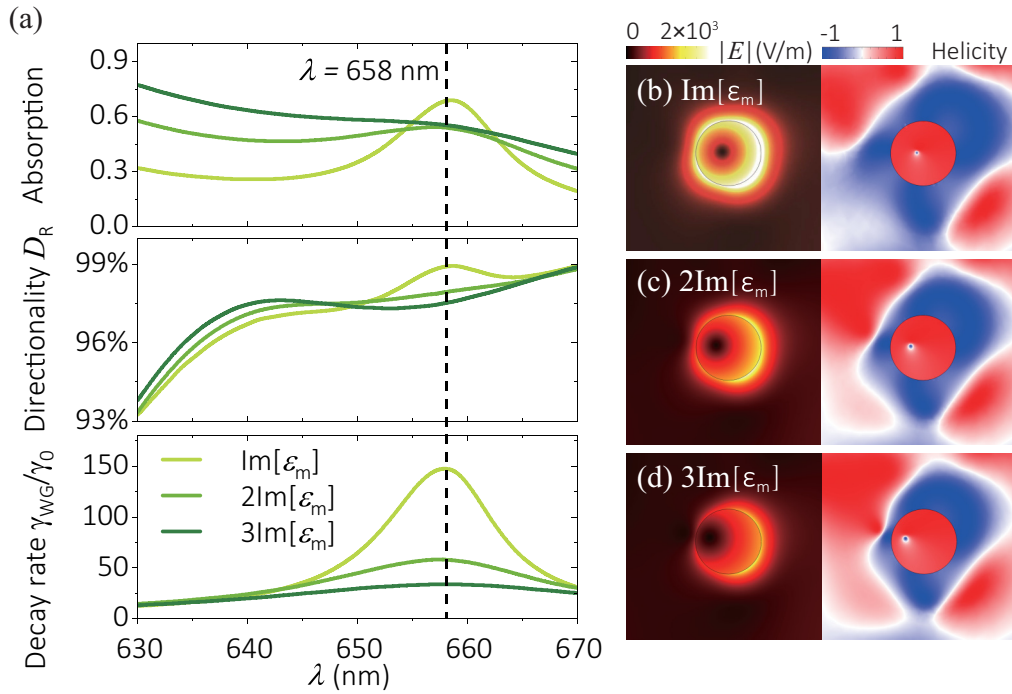


FIG. 11. (a) Absorption spectra, directionality D_R , and normalized decay rate γ_{WG}/γ_0 for $\text{Im}[\epsilon_m]$, $2\text{Im}[\epsilon_m]$, and $3\text{Im}[\epsilon_m]$. Here the imaginary part $\text{Im}[\epsilon_m]$ of the dielectric constant is artificially increased by a factor of 1, 2, and 3, while its real part $\text{Re}[\epsilon_m]$ is kept as the original value for each wavelength. It is seen that increasing the loss of metal material does not obviously affect the peak position and directionality, but does affect the Purcell enhancement. (b)–(d) The electric-field and its helicity distributions around the AgNP with the area of 120×120 nm² for (b) $\text{Im}[\epsilon_m]$, (c) $2\text{Im}[\epsilon_m]$, and (d) $3\text{Im}[\epsilon_m]$. Other parameters are the same as those in Fig. 3.

band edge of the PC. In our system, the maximum γ_{WG}/γ_0 is less than 15 with the directionality of 92% in the case of $y = 50$ nm. While the helicity is ≈ 0 when $y = 0$, the numbers of photons propagating to right and left directions are almost the same, i.e., losing the direction lock of photon propagation.

APPENDIX H: POSITION OPTIMIZATION OF THE EMITTER AND AgNP IN THE COUPLED PC AND AgNP STRUCTURE

To obtain high directionality of photon propagation, in the main paper, we optimize the parameters of the system by

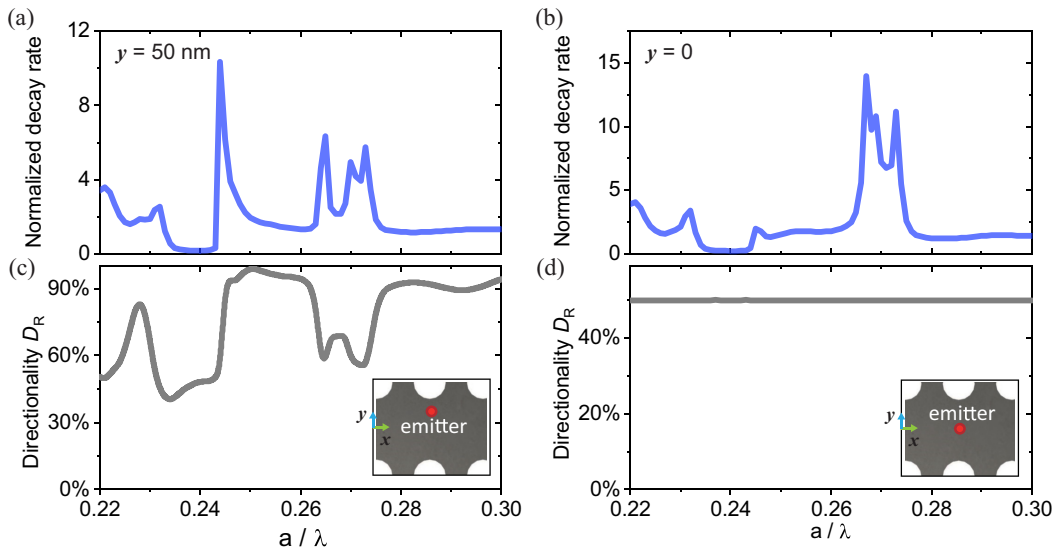


FIG. 12. Total decay rate γ_{tot} normalized by γ_0 of a σ_- emitter embedded in the PC waveguide for (a) $y = 50$ and (b) $y = 0$ nm. $\gamma_{\text{tot}}/\gamma_0$ is almost less than 15 when a/λ is within the guided band [19]. (c), (d) Corresponding directionality D_R for (c) $y = 50$ and (d) $y = 0$ nm. The lattice constant is $a = 190$ nm. Other parameters are the same as those in Fig. 3.

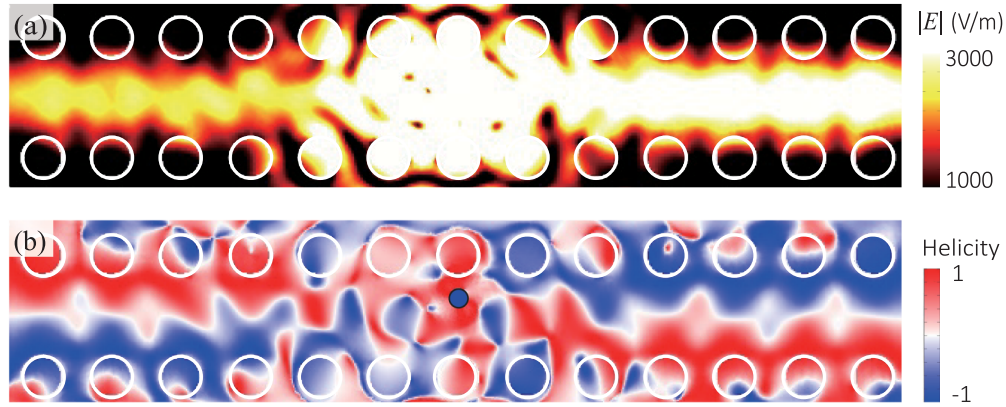


FIG. 13. (a) Electric field and (b) its helicity of the σ_- emitter in the coupled PC and AgNP structure, for $r_m = 20$ nm, $y = 50$ nm, and $\theta = 45^\circ$. The photons propagate to two sides along the waveguide of the PC, leading to small directionality D_R . The symmetry of helicity in both propagating channels is not broken compared with that with $\theta = 180^\circ$ in the main text. Other parameters are the same as those in Fig. 3.

selecting the positions of the emitter around the AgNP. The helicity where the emitter is placed should be large enough to ensure a unidirectional photon propagation. For Fig. 3, the case that $\theta = 180^\circ$ is chosen, the directionality of which is 98%. In contrast, when $\theta = 45^\circ$, the directionality is only 66% due to the small helicity, the electric-field and helicity distributions of which are depicted in Fig. 13.

Moreover, the case that the emitter is placed at the planes of $z \neq 0$ is discussed. For example, the normalized decay rate and directionality of the right-handed polarized emitter σ_- at the top of the AgNP with a distance of 2 nm are shown in Fig. 14. The total decay rate and its guide part are increased less than those in the plane of $z = 0$ and the directionality is only 63.8% at $\lambda = 658$ nm due to the low helicity of 0.6. So the results in Fig. 3 are optimized by the position of the emitter.

As we did for Fig. 4, to find the narrowest linewidth of the band-edge mode [mode 2 in Fig. 2(b)], we change the position of the AgNP from point 1 to point 7 in Fig. 15(a). After comparing the full widths at half maximum of all hybrid modes, we finally place the AgNP at point 6 with the linewidth of $\kappa = 2.9$ meV [Figs. 15(b)–15(h)].

For a σ_+ emitter, to verify the same Purcell enhancement and an opposite photon propagation as those of the σ_- emitter, we compute the normalized decay rates $\gamma_{\text{tot}}/\gamma_0$ and $\gamma_{\text{WG}}/\gamma_0$ and the directionality D_L of the emitted photons as a function of θ and λ [Fig. 16]. Other parameters are the same as those in Fig. 2. As expected, the directionality and decay rates have the same maximal values due to the symmetry. From the helicity distribution, we can see that the symmetry of the propagation to the right direction is broken, which is opposite to that of the σ_- emitter in Fig. 3(d).

APPENDIX I: PARAMETER OPTIMIZATION IN THE COUPLED PC AND Ag NANOBLOCK STRUCTURE

A coupled PC and silver nanoblock structure is capable of separating the photons with different wavelenghtes into opposite propagation directions. As shown in Fig. 17(a), if the AgNP is substituted by a silver nanoblock with the length of 25 nm and height of 10 nm, its optical modes appear at the wavelength of 705 and 639 nm, respectively. Because the helicity has opposite signs around the nanoblock for the two modes [Figs. 17(b) and 17(c)], according to the principle

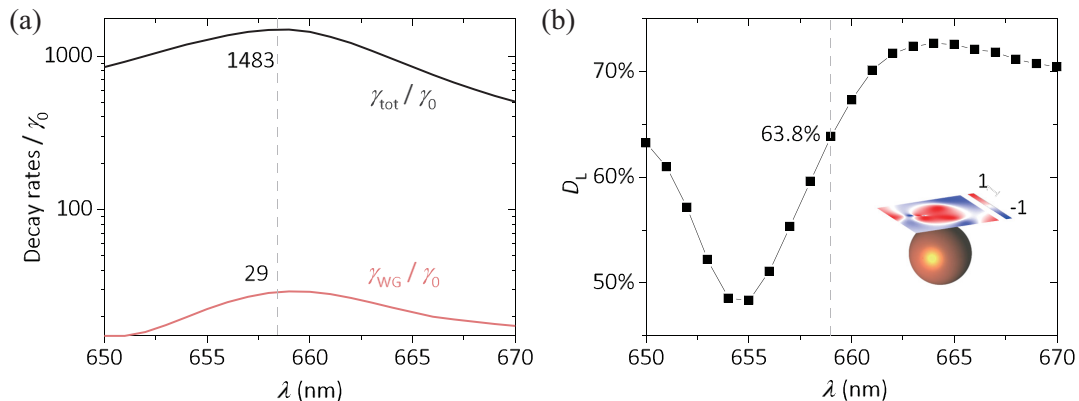


FIG. 14. (a) Normalized decay rates and (b) directionality D_L for a right-handed polarized emitter σ_- placed at the top of the AgNP with $r_m = 20$ nm and a distance of 2 nm. The helicity distribution of the plane with $z = 22$ nm is shown in the inset. At the resonant wavelength of 658 nm, the total decay rate and its guided part are increased less than those in the plane of $z = 0$ and the directionality is only 63.8%. Other parameters are the same as those in Fig. 3.

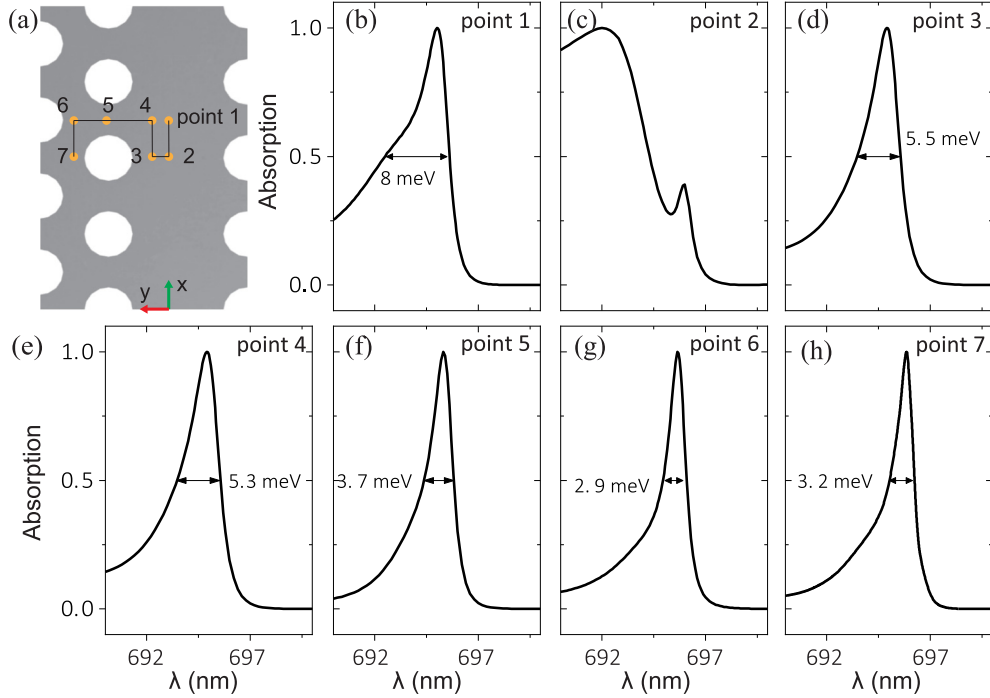


FIG. 15. (a) Schematic diagram of the AgNP with $r_m = 7$ nm located in different positions of the PC with $a = 170$ nm. Supposing the coordinate of point 1 is $(0, 0)$, the coordinates of points 2–7 are $(-0.5a, 0)$, $(-0.5a, 50$ nm), $(0, 50$ nm), $(0, 0.5\sqrt{3}a)$, $(0, 0.75\sqrt{3}a)$, and $(-50$ nm, $0.75\sqrt{3}a)$. (b)–(h) The absorption spectra of the band-edge mode for various AgNP positions marked in (a). The linewidth κ of the AgNP is optimized by selecting its position. In the main text, point 6 with $\kappa = 2.9$ meV is chosen.

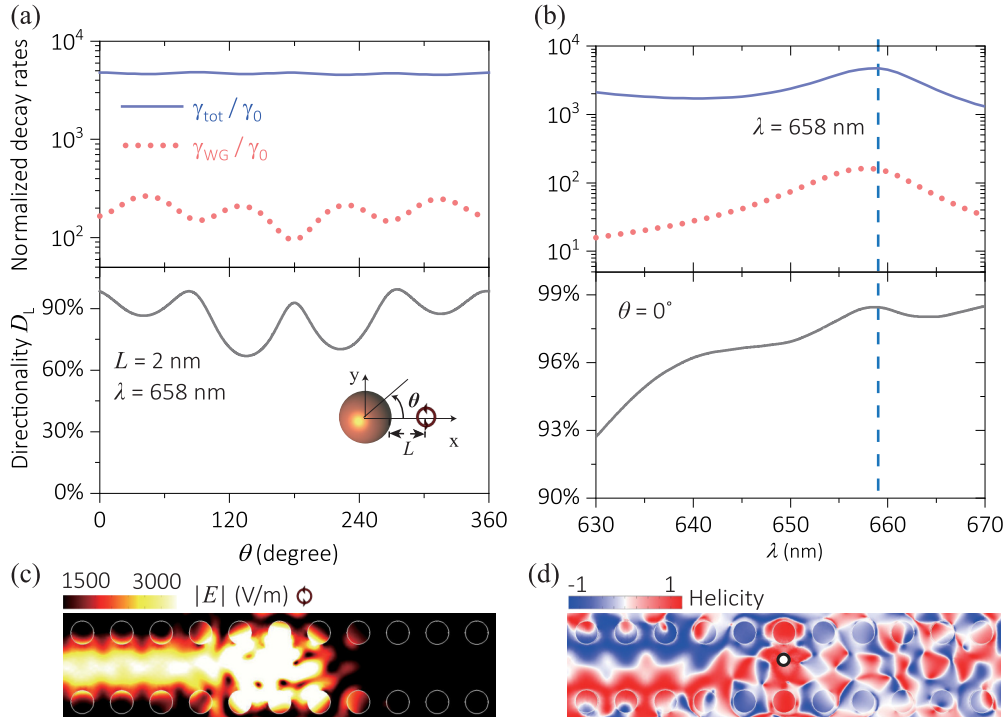


FIG. 16. Normalized decay rates $\gamma_{\text{tot}}/\gamma_0$ and $\gamma_{\text{WG}}/\gamma_0$ of a σ_+ emitter and the directionality D_L of the emitted photons as a function of (a) θ and (b) λ for $a = 190$ nm, $r_m = 20$ nm, and $L = 2$ nm. In (a), the maxima of $\gamma_{\text{WG}}/\gamma_0$ generally corresponds to minima of D_L and vice versa, while $\gamma_{\text{tot}}/\gamma_0$ keeps in a high range of 4600–4800. $\theta = 0^\circ$ is chosen in (b). When $\lambda = 658$ nm, Purcell enhancement reaches $\gamma_{\text{tot}}/\gamma_0 = 4700$ and $\gamma_{\text{WG}}/\gamma_0 = 148$, where 98.4% of emitted photons propagate to the left direction. (c, d) The distributions of (c) the electric field and (d) its helicity when a σ_+ emitter excites the quadrupolar mode of the AgNP. From the helicity distribution, the symmetry of the propagation is broken, which is opposite to that of the σ_- emitter in Fig. 3(d).

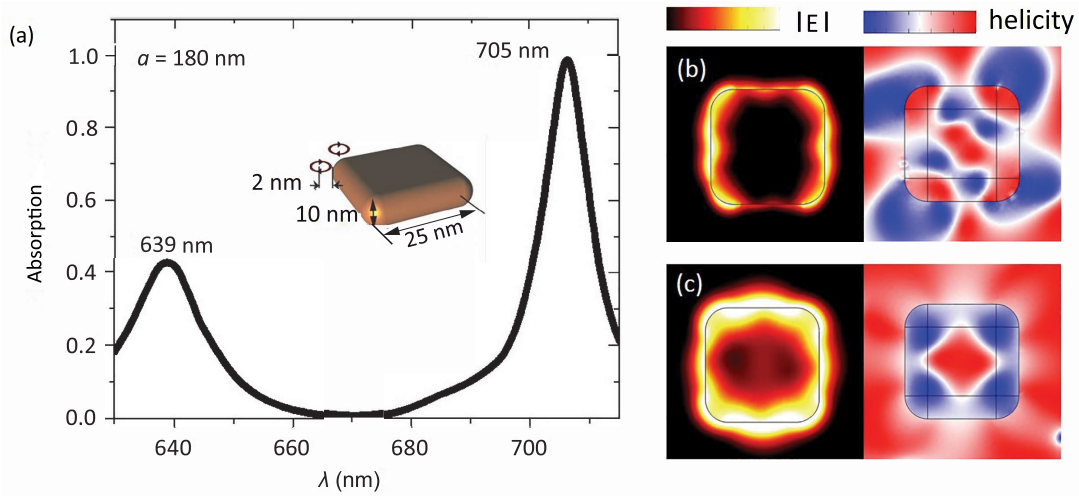


FIG. 17. (a) Absorption spectra of the silver nanoblock embedded in the waveguide of the PC with $a = 180$ nm. Here, the nanoblock with length of 25 nm and height of 10 nm is placed at $y = 50$ nm. (b), (c) The electric-field and helicity distributions for the nanoblock at (b) $\lambda = 639$ nm and (c) $\lambda = 705$ nm.

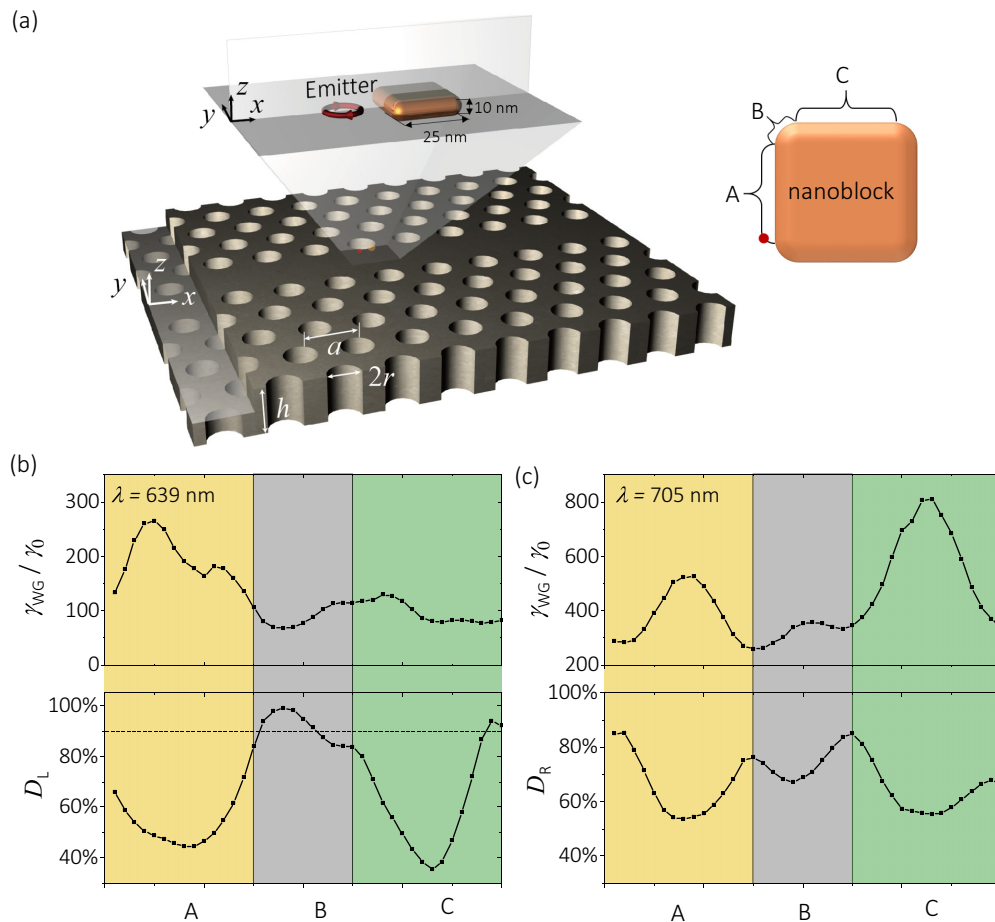


FIG. 18. (a) Schematic diagram of the coupled PC and Ag nanoblock structure. Normalized decay rate γ_{WG}/γ_0 and directionality as a function of the emitter's position, for (b) $\lambda = 639$ nm and (c) $\lambda = 705$ nm. The maximal values of the directionality are 85 and 99% corresponding to $\lambda = 639$ and 705 nm, respectively. Here, the nanoblock is 25 nm in length and 10 nm in height, $a = 178$ nm, $h = 0.84a$, and $r = 0.29a$.

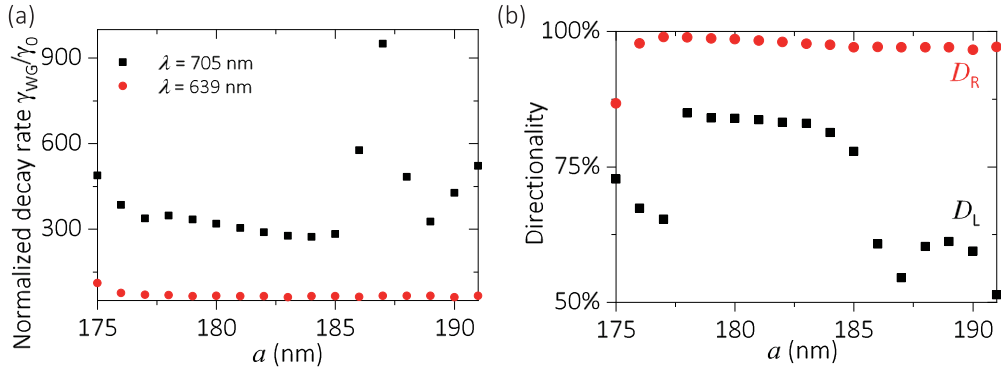


FIG. 19. (a) Normalized decay rates $\gamma_{\text{tot}}/\gamma_0$ and $\gamma_{\text{WG}}/\gamma_0$ of a σ_- emitter and (b) directionality as a function of lattice constant a for $\lambda = 639$ and 705 nm. When $a = 178$ nm, $\gamma_{\text{tot}}/\gamma_0$, $\gamma_{\text{WG}}/\gamma_0$, and directionality are 8079, 307, and 99% for $\lambda = 639$ nm, respectively, and $\gamma_{\text{tot}}/\gamma_0 = 13\,461$, $\gamma_{\text{WG}}/\gamma_0 = 69$, and $D_L = 85\%$ for $\lambda = 705$ nm. Here, for both wavelengths, the emitter is placed at the position with the highest directionality shown in Fig. 18.

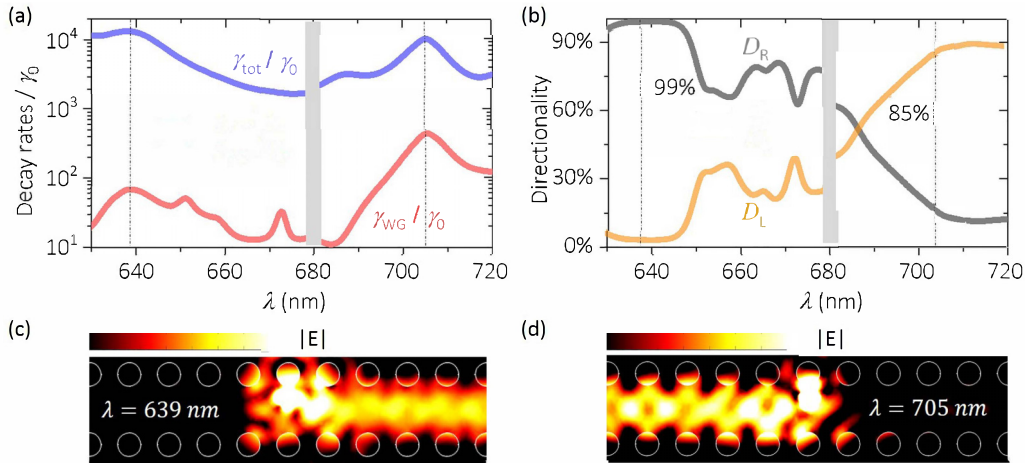


FIG. 20. (a) Normalized decay rates and (b) directionality $D_{R\text{ or }L}$ as a function of λ for two emitters. The emitter is placed in the position with the maximal helicity for each wavelength. (c), (d) The electric field in the waveguide at (c) $\lambda = 639$ nm and (d) $\lambda = 705$ nm. Other parameters are the same as those in Fig. 14.

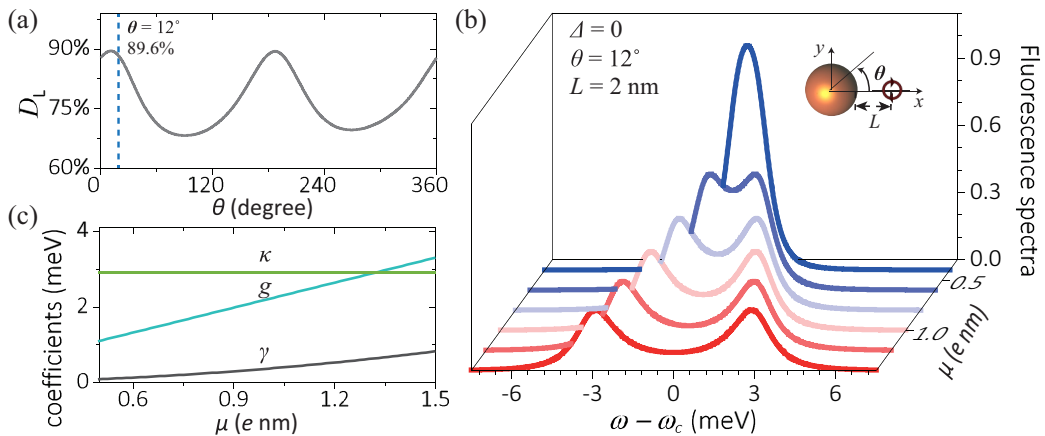


FIG. 21. (a) Directionality D_L of emitted photons dependent on θ . The AgNP with $r_m = 7$ nm is placed at point 6 of Fig. 15. Directionality D_L reaches the maximum when $\theta = 12^\circ$ and 190° with the value of 89.6%. (b) Fluorescence spectra of the quantum emitter as a function of $\omega - \omega_c$ with varying dipole moment μ . The parameters g , γ , κ in dependence on μ are shown in (c). Here, $L = 2$ nm and the detuning Δ between the nanocavity and emitter is zero.

```

1 from qutip import *
2 import numpy as np
3
4 # constant
5 hb = 6.58211899E-13 # Planck constant; Unit: meV*s
6 ep0 = 8.854187817E-12 # the permittivity of vacuum; Unit: F/m
7 el = 1.602176487E-19 # electron charge; unit: C
8 c = 299792458.0E9 # speed of light; Unit: nm/s
9
10 # set frequency
11 lda_c = 695.65 # wavelength of the AgNP; Unit: nm
12 omega_c = 2 * pi * hb * c / lda_c # frequency of the AgNP; Unit: meV
13 mu = 1.0 # dipole moment; Unit: erm
14 omega_a = 2 * pi * hb * c / lda_c + kappa / 2 # frequency of the emitter
15 wlist = linspace(omega_c - 50, omega_c + 50, 10000) # change frequency
16 op = np.array(wlist - omega_c)
17
18 # parameters of g, gamma, kappa
19 kappa = 2.9 # loss of the AgNP; Unit: meV
20 g = 3.14 # coupling coefficient
21 gamma0 = (1 / (4 * pi * ep0)) * (4 * (omega_a / hb)**3 * mu**2 / (3 * c**3)) \
22 * 1.6E-7 # decay rate in vacuue
23 gamma = 416 * gamma0
24
25 # solve EOM
26 N = 2
27 n_th = 1e-4
28
29 a = tensor(destroy(N), qeye(2)) # bosonic annihilation operator
30 sigma = tensor(qeye(N), sigmam())
31 # lowering operator
32 H = omega_c * a.dag() * a + omega_a * sigma.dag() * sigma + \
33 g * (a * sigma.dag() + a.dag() * sigma) # Hamiltonian
34 c_ops = [sqrt(kappa * (1 + n_th)) * a, sqrt(kappa * n_th) * a.dag(), \
35 sqrt(gamma) * sigma] # decay of the system
36
37 # caculate spectra
38 spec = spectrum(H, wlist, c_ops, sigma.dag(), sigma)
39 plot(wlist-omega_c, spec)

```

FIG. 22. The screen shot of the PYTHON program for the resonance fluorescence spectrum of $\mu = 1.0 e \text{ nm}$ in Fig. 4(e).

of chiral coupling, the photons with these two wavelengths emitted from the emitter with the same polarization should be guided to opposite directions. To prove this point, we first optimize the parameters of the PC. The basic requirement here is to transmit photons with the wavelength of 639 and 705 nm simultaneously, so the choice of lattice constant a should make sure that the wavelengths of both photons are within the guided band of the PC, namely, a/λ should be within the range of 0.25–0.3. Thus, after the computation, a corresponds to a range of 176–191 nm.

Figure 18 depicts normalized guided decay rate and directionality of a right-handed polarized emitter σ_- coupled to an Ag nanoblock with the length of 25 nm and the height of 10 nm. The lattice constant a is 178 nm. The distance between the emitter and the surface of the nanoblock is fixed at 2 nm. And the position of the nanoblock is (0, 50 nm, 0) (supposing

the origin of the coordinate is at the center of the PC). After moving the emitter from region A, via region B, to region C, it is seen that the directionality D_L can easily reach 90% at region B for $\lambda = 639 \text{ nm}$. Especially, the maximal D_L is 99% with $\gamma_{WG}/\gamma_0 = 68$, while for $\lambda = 705 \text{ nm}$ the photons are guided to the right direction and the maximal directionality $D_R = 85\%$ with $\gamma_{WG}/\gamma_0 = 346$. Comparing Fig. 18(b) with Fig. 18(c), we find the maximal helicity appears at the corner of the nanoblock at $\lambda = 639 \text{ nm}$, but deviates from the corner at $\lambda = 705 \text{ nm}$, which are coincident with the positions with maximal directionality. Also, the localized electric field at $\lambda = 705 \text{ nm}$ is much stronger than that at the other wavelengths, so a larger decay rate is obtained.

Furthermore, to find out the influence of lattice constant a of the PC, we investigate γ_{WG}/γ_0 of the emitter and directionality of emitted photons at $\lambda = 639$ and 705 nm (Fig. 19).

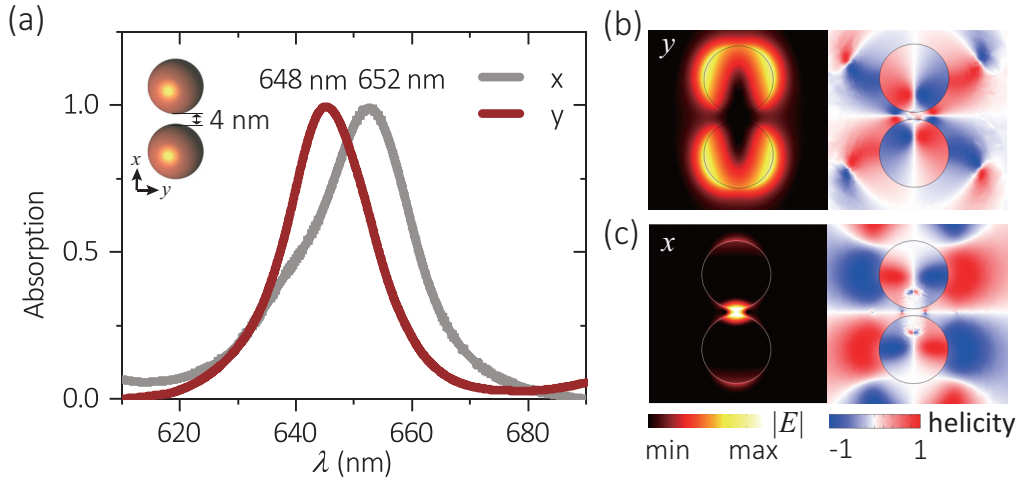


FIG. 23. (a) Normalized absorption spectra of an Ag dimer excited by x and y polarized plane waves. The resonant wavelengths are 652 and 648 nm, respectively. Electric-field and helicity distributions in the cases of a (b) y polarized plane wave and (d) x polarized plane wave. The radii of the AgNPs are 20 nm with a gap distance of 4 nm.

According to the results in Figs. 18(b) and 18(c), the emitter should be placed at the positions where the directionalities reach their maxima for two wavelengths. When $a = 178$ nm, the directionality $D_R = 99\%$ for $\lambda = 639$ nm and $D_L = 85\%$ for $\lambda = 705$ nm, which are both maximal values in their own cases [electric-field distributions are shown in Figs. 20(c) and 20(d)]. Correspondingly, at $\lambda = 639$ nm, the normalized decay rate $\gamma_{WG}/\gamma_0 = 307$, while, at $\lambda = 705$ nm, $\gamma_{WG}/\gamma_0 = 69$ [Figs. 20(a) and 20(b)].

APPENDIX J: FLUORESCENCE SPECTRA OF THE QUANTUM EMITTER

The PYTHON toolbox is performed to derive the resonance fluorescence spectrum of the CQED system by Fourier transformation electric intensity $\langle E^-(\vec{r}, t)E^+(\vec{r}, t) \rangle$, with the expression of $S(\vec{r}, \omega_0) = \frac{1}{\pi} \text{Re} \int d\tau \langle E^-(\vec{r}, t)E^+(\vec{r}, t) \rangle e^{i\omega_0 t}$ [52,53]. By increasing the dipole moment of the emitter, Rabi splitting appears in the fluorescence spectra [Figs. 4(e) and 21]. When the transition frequency of the emitter is resonant with the frequency of the nanocavity, the peaks of Rabi splitting are symmetric (Fig. 21). By contrast, asymmetry of the spectrum occurs as the emitter frequency deviates from that of the nanocavity mode [Fig. 4(e)]. In the following, we present the code and show how to obtain the resonance fluorescence spectrum by means of the PYTHON toolbox.

By importing the QUTIP package [53], some quantum-mechanics operations, such as commutation and solving equation of motion, can be easily done. Note, the operators and Hamiltonian should be expressed by the matrix with the dimension of 2. As shown in Fig. 22, “omega_c” and “omega_a” are the frequencies of the nanocavity and the emitter, with detuning of $\kappa/2$; “kappa,” “gamma,” and “g” are the cavity loss, the decay rate of the emitter, and the coupling coefficient between the nanocavity and the emitter. We let the thermal environment be characterized by an average particle expectation value of $\langle n \rangle = n_{\text{th}}$. The dynamics of the system can be written as $\dot{\rho} = i[\rho, H]/\hbar - \Gamma(\rho)$. Here

the Hamiltonian and the system decay Γ are represented by “H” and “c_ops.” Then the spectra are calculated by the correlation function using the mesolve solver in the QUTIP package, and then obtained by Fourier transform. Finally, we give an example of the PYTHON program for the resonance fluorescence spectrum of $\mu = 1.0 e \text{ nm}$ in Fig. 4(e) (see the screen shot in Fig. 22).

APPENDIX K: DIMER PLASMON NANOSTRUCTURE

Dimer plasmon nanostructures are widely used to enhance the Purcell factor because of the ultralarge electric-field enhancement within the nanoscale gap [54,55]. To investigate the directionality of photons in coupled PC and AgNP dimer structure, we first explore the optical modes of only the dimer structure with the radius of 20 nm and the gap distance of 4 nm. The x - and y -polarized plane waves are used to excite the AgNP dimer [inset of Fig. 23(a)], where x -polarized light polarizes parallel to the axis of the dimer and y -polarized light is perpendicular to it. Corresponding to these two excitons, the resonant wavelengths of 652 and 648 nm are obtained (Fig. 23). Figures 23(b) and 23(c) show their electric-field and helicity distributions. It is seen that x -polarized light is able to excite the gap surface plasmon, while by using y -polarized light the electric field distributes around the dimer. Importantly, in both cases, the helicity within the gap is almost zero. If the incident light is changed to a circularly polarized wave, the obtained mode is the superposition of these modes, thus the helicity within the gap is still almost zero.

Then a coupled PC and AgNP dimer structure is considered, where a right-handed polarized emitter σ_- is put at the center of the gap. Both the dimer and the emitter are embedded in the middle plane of the PC [Fig. 24(a)]. We obtain the decay rate γ_{WG}/γ_0 of the emitter and the directionality D_L of photon propagation with varying the wavelength of the emitter [Fig. 24(c)]. It is seen that the resonant wavelength of the dimer is 652 nm, which means that the coupled mode is mainly excited by the electric-field component that is parallel

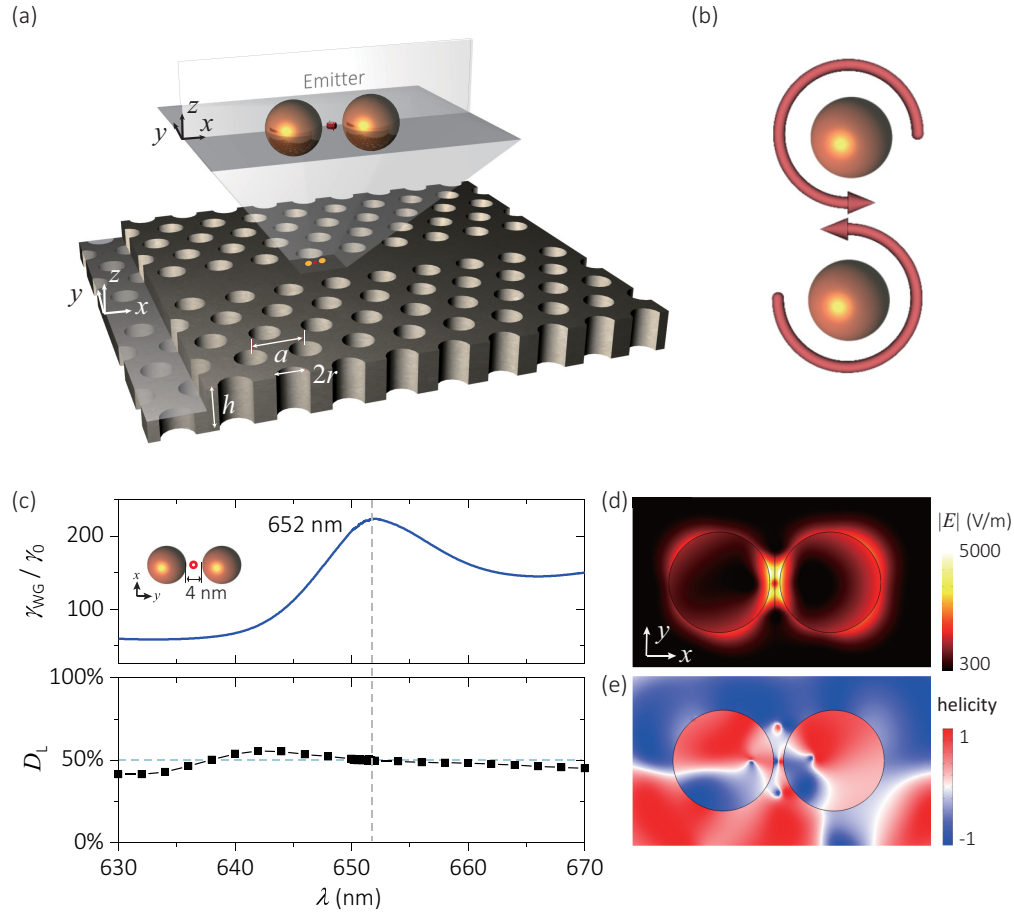


FIG. 24. (a) Schematic diagram of the coupled PC and AgNP dimer structure. (b) Schematic diagram of the polarization ellipses of the electric fields around the AgNPs. (c) Normalized decay rate $\gamma_{\text{WG}}/\gamma_0$ of a σ_- emitter and the directionality D_L of the emitted photons as a function of λ . At the resonant wavelength of $\lambda = 652$ nm, $\gamma_{\text{WG}}/\gamma_0$ reaches maximum while $D_L = 49.5\%$. (d) Electric-field and (e) helicity distributions of the AgNP dimer. The parameters of the PC are the same as those in Fig. 5 and those of the AgNP dimer are the same as those in Fig. 23.

to the axis of the dimer. At $\lambda = 652$ nm, the decay rate of the guided part $\gamma_{\text{WG}}/\gamma_0$ is 225 with $D_L = 49.5\%$. To explain the results, Figs. 24(d) and 24(e) depict the electric-field and helicity distributions of the dimer within an area of 120×60 nm², where the electric field in the gap is greatly enhanced while the helicity is almost near zero, leading to the large Purcell enhancement but a bidirectional photon propagation.

The reason for bidirectional propagation is described as follows. The symmetry structure generally destroys the helicity of the local field [Fig. 24(b)]. For the nanoparticle dimer, the electric field for each particle has the same handedness, so within the gap region the polarization ellipses of the electric fields counteract each other, leading to near-zero helicity. In general, this result is suitable for general dimer nanostructures, such as the bowtie structure and nanosphere dimer.

- [1] S. Haroche and D. Kleppner, Cavity quantum electrodynamics, *Phys. Today* **42**, 24 (1989).
- [2] R. Miller, T. E. Northup, K. M. Birnbaum, A. Boca, A. D. Boozer, and H. J. Kimble, Trapped atoms in cavity QED: Coupling quantized light and matter, *J. Phys. B* **38**, S551 (2005).
- [3] K. J. Vahala, Optical microcavities, *Nature (London)* **424**, 839 (2005).
- [4] H. Walther, B. T. H. Varcoe, B.-G. Englert, and T. Becker, Cavity quantum electrodynamics, *Rep. Prog. Phys.* **69**, 1325 (2006).
- [5] H. J. Kimble, Strong interactions of single atoms and photons in cavity QED, *Phys. Scr.* **T76**, 127 (1998).
- [6] T. Yoshie, A. Scherer, J. Hendrickson, G. Khitrova, H. M. Gibbs, G. Rupper, C. Ell, O. B. Shchekin, and D. G. Deppe, Vacuum Rabi splitting with a single quantum dot in a PC nanocavity, *Nature (London)* **432**, 200 (2004).
- [7] Y. Akahane, T. Asano, B.-S. Song, and S. Noda, High-Q photonic nanocavity in a two-dimensional PC, *Nature (London)* **425**, 944 (2003).
- [8] R. Chikkaraddy, B. de Nijs, F. Benz, S. J. Barrow, O. A. Scherman, E. Rosta, A. Demetriadou, P. Fox, O. Hess, and

- J. Baumberg, Single-molecule strong coupling at room temperature in plasmonic nanocavities, *Nature (London)* **535**, 127 (2016).
- [9] C. Sauvan, J. P. Hugonin, I. S. Maksymov, and P. Lalanne, Theory of the Spontaneous Optical Emission of Nanosize Photonic and Plasmon Resonators, *Phys. Rev. Lett.* **110**, 237401 (2013).
- [10] G. M. Akselrod, C. Argyropoulos, T. B. Hoang, C. Ciraci, C. Fang, J. Huang, D. R. Smith, and M. H. Mikkelsen, Probing the mechanisms of large Purcell enhancement in plasmonic nanoantennas, *Nat. Photonics* **8**, 835 (2014).
- [11] K. J. Russell, T.-L. Liu, S. Cui, and E. L. Hu, Large spontaneous emission enhancement in plasmonic nanocavities, *Nat. Photonics* **6**, 459 (2012).
- [12] C. Junge, D. O'Shea, J. Volz, and A. Rauschenbeutel, Strong Coupling Between Single Atoms and Nontransversal Photons, *Phys. Rev. Lett.* **110**, 213604 (2013).
- [13] O. Benson, Assembly of hybrid photonic architectures from nanophotonic constituents, *Nature (London)* **480**, 193 (2011).
- [14] M. Kamandar Dezfouli, R. Gordon, and S. Hughes, Modal theory of modified spontaneous emission of a quantum emitter in a hybrid plasmonic photonic-crystal cavity system, *Phys. Rev. A* **95**, 013846 (2017).
- [15] H. Lian, Y. Gu, J. Ren, F. Zhang, L. Wang, and Q. Gong, Efficient Single Photon Emission and Collection Based on Excitation of Gap Surface Plasmons, *Phys. Rev. Lett.* **114**, 193002 (2015).
- [16] J. Ren, Y. Gu, D. Zhao, F. Zhang, T. Zhang, and Q. Gong, Evanescent-Vacuum-Enhanced Photon-Exciton Coupling and Fluorescence Collection, *Phys. Rev. Lett.* **118**, 073604 (2017).
- [17] H. J. Kimble, The quantum internet, *Nature (London)* **453**, 1023 (2008).
- [18] J. Petersen, J. Volz, and A. Rauschenbeutel, Chiral nanophotonic waveguide interface based on spin-orbit interaction of light, *Science* **346**, 67 (2014).
- [19] S. Mahmoodian, K. Prindal-Nielsen, I. Söllner, S. Stobbe, and P. Lodahl, Engineering chiral light-matter interaction in PC waveguides with slow light, *Opt. Mater. Express*, **7**, 43 (2017).
- [20] S.-H. Gong, F. Alpeggiani, B. Sciacca, E. C. Garnett, and L. Kuipers, Nanoscale chiral valley-photon interface through optical spin-orbit coupling, *Science* **359**, 443 (2018).
- [21] F. J. Rodríguez-Fortuño, G. Marino, P. Ginzburg, D. O'Connor, A. Martínez, G. A. Wurtz, and A. V. Zayats, Near-field interference for the unidirectional excitation of electromagnetic guided modes, *Science* **340**, 328 (2013).
- [22] L. Marrucci, Quantum optics: Spin gives direction, *Nat. Phys.* **11**, 9 (2014).
- [23] P. Lodahl, S. Mahmoodian, S. Stobbe, A. Rauschenbeutel, P. Schneeweiss, J. Volz, H. Pichler, and P. Zoller, Chiral quantum optics, *Nature (London)* **541**, 473 (2017).
- [24] A. B. Young, A. C. T. Thijssen, D. M. Beggs, P. Androvitsaneas, L. Kuipers, J. G. Rarity, S. Hughes, and R. Oulton, Polarization Engineering in PC Waveguides for Spin-Photon Entanglers, *Phys. Rev. Lett.* **115**, 153901 (2015).
- [25] C. Gonzalez-Ballester, A. Gonzalez-Tudela, F. J. Garcia-Vidal, and E. Moreno, Chiral route to spontaneous entanglement generation, *Phys. Rev. B* **92**, 155304 (2015).
- [26] I. Söllner, S. Mahmoodian, S. L. Hansen, L. Midolo, A. Javadi, G. Kiršanskė, T. Pregolato, H. El-Ella, E. H. Lee, J. D. Song, S. Stobbe, and P. Lodahl, Deterministic photon-emitter coupling in chiral photonic circuits, *Nat. Nanotechnol.* **10**, 775 (2015).
- [27] T. C. Ralph, I. Söllner, S. Mahmoodian, A. G. White, and P. Lodahl, Photon Sorting, Efficient Bell Measurements, and a Deterministic Controlled-Z Gate Using a Passive Two-Level nonlinearity, *Phys. Rev. Lett.* **114**, 173603 (2015).
- [28] I. Shomroni, S. Rosenblum, Y. Lovsky, O. Bechler, G. Guendelman, and B. Dayan, All-optical routing of single photons by a one-atom switch controlled by a single photon, *Science* **345**, 903 (2014).
- [29] C. Sayrin, C. Junge, R. Mitsch, B. Albrecht, D. O'Shea, P. Schneeweiss, J. Volz, and A. Rauschenbeutel, Nanophotonic Optical Isolator Controlled by the Internal State of Cold Atoms, *Phys. Rev. X* **5**, 041036 (2015).
- [30] M. Scheucher, A. Hilico, E. Will, J. Volz, and A. Rauschenbeutel, Quantum optical circulator controlled by a single chirally coupled atom, *Science* **354**, 1577 (2016).
- [31] A. Kuhn, M. Hennrich, and G. Rempe, Deterministic Single-Photon Source for Distributed Quantum Networking, *Phys. Rev. Lett.* **89**, 067901 (2002).
- [32] S. Nußmann, M. Hijlkema, B. Weber, F. Rohde, G. Rempe, and A. Kuhn, Submicron Positioning of Single Atoms in A Microcavity, *Phys. Rev. Lett.* **95**, 173602 (2005).
- [33] T. Wilk, S. C. Webster, H. P. Specht, G. Rempe, and A. Kuhn, Polarization-Controlled Single Photons, *Phys. Rev. Lett.* **98**, 063601 (2007).
- [34] A. D. Boozer, A. Boca, R. Miller, T. E. Northup, and H. J. Kimble, Reversible State Transfer Between Light and A Single Trapped Atom, *Phys. Rev. Lett.* **98**, 193601 (2007).
- [35] T. Aoki, A. S. Parkins, D. J. Alton, C. A. Regal, B. Dayan, E. Ostby, K. J. Vahala, and H. J. Kimble, Efficient Routing of Single Photons by One Atom and a Microtoroidal Cavity, *Phys. Rev. Lett.* **102**, 083601 (2009).
- [36] D. O'Connor, P. Ginzburg, F. J. Rodríguez-Fortuño, G. A. Wurtz, and A. V. Zayats, Spin-orbit coupling in surface plasmon scattering by nanostructures, *Nat. Commun.* **5**, 5327 (2014).
- [37] P. Lodahl, S. Mahmoodian, and S. Stobbe, Interfacing single photons and single quantum dots with photonic nanostructures, *Rev. Mod. Phys.* **87**, 347 (2015).
- [38] B. le Feber, N. Rotenberg, and L. Kuipers, Nanophotonic control of circular dipole emission, *Nat. Commun.* **6**, 6695 (2015).
- [39] R. J. Coles, D. M. Price, J. E. Dixon, B. Royall, E. Clarke, P. Kok, M. S. Skolnick, A. M. Fox, and M. N. Makhonin, Chirality of nanophotonic waveguide with embedded quantum emitter for unidirectional spin transfer, *Nat. Commun.* **7**, 11183 (2016).
- [40] M. Arcari, I. Sollner, A. Javadi, S. LindskovHansen, S. Mahmoodian, J. Liu, H. Thyrestrup, E. H. Lee, J. D. Song, S. Stobbe, and P. Lodahl, Near-Unity Coupling Efficiency of a Quantum Emitter to a Photonic-Crystal Waveguide, *Phys. Rev. Lett.* **113**, 093603 (2014).
- [41] H. J. Carmichael, *Statistical Methods in Quantum Optics*, (Springer-Verlag, Berlin, 2008), Vol. 2.
- [42] T. K. Hakala, J. J. Toppari, A. Kuzyk, M. Pettersson, H. Tikkanen, H. Kunttu, and P. Torma, Vacuum Rabi Splitting and Strong-Coupling Dynamics for Surface-Plasmon Polaritons and Rhodamine 6G Molecules, *Phys. Rev. Lett.* **103**, 053602 (2009).
- [43] M. D. Birowosuto, A. Yokoo, G. Zhang, K. Tateno, E. Kuramochi, H. Taniyama, M. Takiguchi, and M. Notomi,

- Movable high-Q nanoresonators realized by semiconductor nanowires on a Si PC platform, *Nat. Mater.* **13**, 279 (2014).
- [44] R. Mitsch, C. Sayrin, B. Albrecht, P. Schneeweiss, and A. Rauschenbeutel, Quantum state-controlled directional spontaneous emission of photons into a nanophotonic waveguide, *Nat. Commun.* **5**, 5713 (2014).
- [45] P. B. Johnson and R. W. Christy, Optical constants of the noble metals, *Phys. Rev. B* **6**, 4370 (1972).
- [46] A. Ridolfo, O. Di Stefano, N. Fina, R. Saija, and S. Savasta, Quantum Plasmonics with Quantum Dot-Metal Nanoparticle Molecules: Influence of the Fano Effect on Photon Statistics, *Phys. Rev. Lett.* **105**, 263601 (2010).
- [47] S. Hughes, L. Ramunno, J. F. Young, and J. E. Sipe, Extrinsic Optical Scattering Loss in Photonic Crystal Waveguides: Role of Fabrication Disorder and Photon Group Velocity, *Phys. Rev. Lett.* **94**, 033903 (2005).
- [48] Y. Ekinici, H. H. Solak, and J. F. Löffler, Plasmon resonances of aluminum nanoparticles and nanorods, *J. Appl. Phys.* **104**, 083107 (2008).
- [49] N. Lukas and H. Bert, *Principles of Nano-Optics* (Cambridge University, Cambridge, England, 2012).
- [50] K. Słowik, R. Filter, J. Straubel, F. Lederer, and C. Rockstuhl, Strong coupling of optical nanoantennas and atomic systems, *Phys. Rev. B* **88**, 195414 (2013).
- [51] A. B. Evlyukhin, G. Brucoli, L. Martín-Moreno, S. I. Bozhevolnyi, and F. J. García-Vidal, Surface plasmon polariton scattering by finite-size nanoparticles, *Phys. Rev. B* **76**, 075426 (2007).
- [52] M. O. Scully and M. S. Zubairy, *Quantum Optics* (Cambridge University, Cambridge, England, 2006).
- [53] J. R. Johansson, P. D. Nation, and F. Nori, QuTiP 2: A Python framework for the dynamics of open quantum systems, *Comput. Phys. Commun.* **184**, 1234 (2013).
- [54] J. B. Lassiter, F. McGuire, J. J. Mock, C. Cirací, R. T. Hill, B. J. Wiley, A. Chilkoti, and D. R. Smith, Plasmonic waveguide modes of film-coupled metallic nanocubes, *Nano Lett.* **13**, 5866 (2013).
- [55] C. E. Talley, J. B. Jackson, C. Oubre, N. K. Grady, C. W. Hollars, S. M. Lane, T. R. Huser, P. Nordlander, and N. J. Halas, Surface-enhanced Raman scattering from individual Au nanoparticles and nanoparticle dimer substrates, *Nano Lett.* **5**, 1569 (2005).